Doctoral Thesis

博士論文

Predicting Local Climate Change in Snow-Covered Regions with High-Resolution Regional Climate Models

（高解像度地域気候モデルを用いた積雪地域の局地的な気候変動予測）

Masaya Nosaka

野坂　真也

令和 4 年

Doctoral Thesis
博士論文

Predicting Local Climate Change in Snow-Covered Regions with High-Resolution Regional Climate Models

（高解像度地域気候モデルを用いた積雪地域の局地的な気候変動予測）

東北大学大学院理学研究科
地球物理学専攻

Masaya Nosaka
野坂　真也

論文審査委員

山崎　剛　教授（主査）
早坂　忠裕　教授
森本　真司　教授
伊藤　純至　准教授
岩崎　俊樹　名誉教授

2022
令和 4 年

Abstract

Global warming has become apparent in the current climate and affected the extreme events such as heavy rainfall. In the future, global warming will continue and accelerate depending on the emission scenario. In order to take countermeasures against global warming, it is important to assess the future changes in regional climates under the much warmer condition. The Meteorological Research Institute (MRI) has provided several datasets based on future climate simulations using the Meteorological Research Institute atmospheric general circulation model (MRI-AGCM) and the Non-Hydrostatic Regional Climate Model (NHRCM). These datasets can be used for studying changes in meteorological phenomena in the warmer climate. The author has involved in the designing and conducting future climate simulation using NHRCM for creating the datasets. Also, the author has analyzed the datasets and clarified the mechanism of future changes in air temperature, precipitation, wind, and snow cover in Japan.

It is important to know the response of surface air temperature (SAT) and precipitation to global warming on a regional scale over Japan. The database for policy making on future climate change (d4PDF) is a dataset of large ensemble climate experiments and used for analyzing future climate changes in SAT and precipitation. However, the d4PDF only assumes +2K and +4K climate compared to the pre-industrial period. We conducted additional ensemble experiment when the global mean temperature increases by 1.5 K using the NHRCM with a 20 km grid spacing, which is a subset of the d4PDF. The reproducibility of the current climate experiment of d4PDF is sufficient to study the future climate change over Japan, and the dynamic downscaling using NHRCM from the global climate model improves the frequency of strong daily precipitation.

Comparing the present-climate, +1.5K +2K, and +4K experiments, the SAT over Japan will increase linearly and faster than the global mean SAT. As warming progresses, the contrast in SST increase over time will become more pronounced. The increase in temperature due to global warming in the annual minimum SAT is larger than that in the average SAT and also that in the annual maximum SAT. Winter precipitation decreases and increases linearly in western and eastern Japan, respectively, reflecting the weakening of the winter monsoon. The annual maximum of daily precipitation (R1d) increases almost linearly with the rise in global SAT, whereas annual precipitation remains almost unchanged. The number of days with strong precipitation will increase as temperatures rise. The number of days without precipitation also increases with increasing temperature. The pattern of precipitation change in the Japanese Islands is highly correlated with that of change in annual mean precipitation and seasonal precipitation excluding summer. The pattern of precipitation change was shown to be responsive to the defined future trend pattern of sea surface temperature. The number of days of snow cover decreases with increasing global temperature at a rate greater than a linear trend. When changes in the global mean temperature range from +1.5K to +2K, R1d increases by 2.7% in the Japanese Islands, although it varies with region. In northern Japan, where the increase in SAT is

large, the increase in R1d is 5%.

The model with 20 km horizontal grid spacing is a coarse resolution for the representation of snow depth because this resolution cannot adequately represent the elevation of each point, making it difficult to project snow depth, which is highly dependent on elevation. NHRCM with 5 km horizontal resolution was used to simulate snow depth in Japan and project future changes in snow depth. The simulated snow depths had biases even at 5 km resolution, and bias correction was necessary to accurately project the future snow depths. Therefore, we developed a new method of bias correction that can produce accurate snow depth and can be easily automated on a computer. Three classification methods of regional frequency analysis were tested in nine regions of Japan; the classification method based on the second order of L-moment (L-cv) was the best bias correction method among those tested. We confirmed that this bias correction is a useful method for projecting future climate, considering estimates from the test sample. In the future climate, the snow depth was projected to decrease by about 50 cm, and the average snow depth in Japan was projected to be about 30 cm. The decrease in maximum snow depth was projected to be larger in Nagano and Gifu and smaller in Hokkaido than in other regions.

The 5 km horizontal resolution model had a snow cover bias and was used for future projections after correcting for data from AMeDAS sites. The 2 km resolution model can reproduce the terrain better and represent convection, which improve the reproduction of weather elements and snow cover. We use the NHRCM with 2 km horizontal resolution to investigate the effect of reduced snow cover on near-surface wind speeds over complex terrain in Japan under a global warming scenario. On synoptic scales, global warming weakens the winter monsoon, which in turn weakens near-surface winds around Japan. Global warming due to climate change reduces Japan's snowpack. Reductions in snow cover drive localized acceleration of rising surface temperatures and prevent the formation of a stable atmospheric boundary layer. When the stable boundary layer collapses, the wind speed and temperature near the surface increase due to the enhancement of momentum and heat exchange with the upper atmosphere. This effect is stronger at low elevations. However, this situation does not occur at high elevations where there is no stable layer under current climate conditions, despite increased ground warming due to reduced snow cover under global warming conditions. An originally stable near-surface atmospheric layer under current climate conditions can therefore influence future changes in wind speed and surface air temperature in snow-covered areas. This mechanism is also confirmed by current climatic observations, which show that wind speeds in the absence of the winter monsoon are stronger on days when there is no snow cover rather than on days with snow cover.

This study, using a regional climate model, has contributed to our understanding of climate change in Japan. The datasets used in these studies were provided to the "JMA Global Warming Projection No. 9" published by the Japan Meteorological Agency. It has also been used for flood control planning by the Ministry of Land, Infrastructure, Transport and Tourism. In "Climate Change in Japan 2020"

published by the Ministry of Education, Culture, Sports, Science and Technology and the Japan Meteorological Agency, in addition to the utility of the dataset, some of the research results were published.

Biases in regional climate model simulations has been reduced significantly with the progress of horizontal resolution. Reducing biases and improving the reproducibility are issues that need to be solved continuously because biases still exist. In addition, it is important to proceed with calculations with increasing ensembles to address uncertainties due to models and SSTs.

Contents

Abstract i
Contents iv
Acknowledgments vi
Chapter 1. Introduction 1
Chapter 2. Scalability of future climate changes across Japan examined with large-ensemble simulations at + 1.5 K, +2 K, and + 4 K global warming levels. 4
2.1 Introduction 4
2.2 Experimental design 5
2.3Results and Discussion 6
2.3.1Reproducibility of the present climate over the Japanese region 6
2.3.2 Future changes in SATs 10
2.3.3 Future changes in Precipitation 14
2.3.4 Future changes in snow covert distribution 24
2.3.5 Impacts of a 0.5 degree increase on regional climates 24
2.4 Conclusions 26
Chapter 3. Bias Correction of Snow Depth by using Regional Frequency Analysis in the Non-Hydrostatic Regional Climate Model around Japan 28
3.1 Introduction 28
3.2 Experimental design and reproducibility of the NHRCM 29
3.3 Methodology of bias correction 30
3.4 Results 33
3.5 Conclusion 36
Chapter 4. Future changes in early spring wind speed and surface warming acceleration in snow-covered areas 37
4.1 Introduction 37
4.2 Methods 38
4.2.1 Model and experimental design 38
4.2.2 Performance of the NHRCM02 39
4.3 Future changes in wind speed 41
4.3.1 Future changes in wind speed over snow-covered areas 41
4.3.2 Impact of changes in synoptic-scale atmospheric circulation on wind speed over snow-covered areas 44
4.4 Mechanisms for projected future wind strengthening 46
4.5 Hypothesis verification and discussion 49
4.5.1 Future changes in daytime and nighttime wind speed 49

4.5.2 Verification using observation data 51
4.5.3 Impact of snow cover on local wind system 52
4.5.4 Summarized processes of future changes in surface wind speed over snowy areas 53
4.6 Conclusions 54
Chapter 5 Conclusion 56
Reference 58

Acknowledgements

I express my sincere thanks to Prof. Takeshi Yamazaki for his useful comments and helpful supports. He carefully commented on this study and provided support for its submission.

I also thank to the members of Meteorological Research Institute. Dr. Hidetaka Sasaki, Dr. Akihiko Murata, Dr. Hiroaki Kawase, Dr. Masayoshi Ishii, and other members gave me the very helpful comments.

Finally, I would like to thank my wife and son for their supporting me mentally.

Chapter 1. Introduction

Global temperature has recorded a rapid increase because of human activities since the industrial revolution. Consequently, an increase in large-scale precipitation events and a decrease in ice sheets and sea ice have been reported (Collins et al. 2013). Predicting future climate change is a major concern if global warming continues.

Numerical prediction models are used in the study of global warming. Global climate models (GCMs) calculate the entire globe and predict global climate change. Studies using GCM have been published, including 60-km-resolution datasets, such as UKCP18 (Met Office Hadley Centre, 2018) and d4PDF. For higher-resolution datasets, the SOUSEI/TOUGOU dataset (Mizuta et al. 2017) has a 20-km resolution, and a study using NICAM was conducted with a 14-km horizontal resolution for 20 years (Kodama et al. 2015). Some studies using global models have performed calculations at subkilometer resolutions (Miyamoto et al. 2013), but in climate research fields, the resolution is coarse because of long-term calculations. Studies using GCMs, for example, predict changes in the circulation field due to global warming and predict the weakening of the East Asian monsoon (Kimoto 2005, Hori and Ueda 2006). Additionally, future drought risk was projected to vary greatly with warming levels using a GCM (Shiogama et al. 2019). However, high-resolution GCMs are problematic because they are computationally expensive and disallow large ensembles.

A regional climate model can save computer resources and can increase the resolution by limiting the region where the downscaling calculation is conducted by obtaining the boundary conditions from the GCM. The increased resolution is useful for reproducing phenomena, such as those caused by topography. Takemi (2013) showed that a detailed topographic representation is important for reproducing wind. Furthermore, Mott et al. (2018) showed that topography is important for reproducing snow cover conditions. Studies using downscaling with regional climate models project longer Mediterranean droughts and increased frequency of high wind events in Europe in the future (Benison et al. 2007). Moreover, Salathé et al. (2010) downscaled, using a regional climate model, Washington State from two global models and reported that global warming effects were commonly projected as an increase in intense precipitation and a decrease in snow cover, although average precipitation was projected to be somewhat different.

In Japan, regional climate projections have been performed by sampling downscaling in Hokkaido (Kuno and Inatsu 2014) and pseudo-warming downscaling experiments (Kawase et al. 2012). Moreover, Nishimori et al. (2019) developed a dataset of regional climate projection scenarios for Japan by statistically downscaling from a global model to reduce bias. Statistical downscaling is computationally inexpensive and reproduces climate values well; however, the physical processes are oversimplified and lack physical plausibility. More so, the reproducibility of each climate element is efficient with dynamical downscaling (Iizumi et al. 2011). Datasets such as those produced in Japan

so far are statistical downscaling methods or cover a part of Japan. Thus, no high-resolution dynamic downscaling datasets cover Japan and have been computed over a long period.

The meteorological research institute (MRI) has been producing various future climate projection datasets using a dynamical downscaling system based on the GCM MRI-AGCM and the regional climate model called nonhydrostatic regional climate model (NHRCM; Table 1). The author was involved in the NHRCM data preparation for the datasets. For the regional climate change projection dataset, the author was involved in constructing the experimental environment. For the d4PDF dataset, the author was an executor of the current climate and 4-K rise experiments. In the 1.5-K rise experiment, both the global and domain model runs were performed by the author. Various studies have been conducted using these AGCM-NHRCM datasets: Kawase et al. (2020a) used the d4PDF dataset to show that future warming reduces the average snowfall but intensifies extreme heavy snowfall. Murata et al. (2017) showed that strong precipitation over Hokkaido further intensifies by future convergence changes using the SOUSEI/TOUGOU dataset. Mori et al. (2019), using the d4PDF dataset, projected a 0.3- to 0.45-m rise in the 100-year storm surge in Tokyo and Osaka bays when the temperature rises to 4 K from pre-industrial levels. Additionally, these data have been used as the basis for reports issued by government agencies, such as the Japan Meteorological Agency's Global Warming Prediction Information, Japan's Climate Change 2020, and the Ministry of the Environment's Japan's Climate in the 21st Century, and for flood control planning by the Ministry of Land, Infrastructure, Transport and Tourism.

Table 1. Examples of NHRCM dataset.

Dataset	Global warming scenario	Global warming levels	GCM horizontal resolution (km)	RCM horizontal resolution (km)	Number of ensembles
JMA Global Warming Prediction No. 8	A1B	Near future End of the 21st century	20	5	1
MOEJ and JMA Regional Climate Change Projection Data	RCP2.6, 4.5, 6.0, 8.5	End of the 21st century	60	20	20
SOUSEI/TOUGOU	RCP2.6, 8.5	End of the 21st century	20	5 or 2	4
database for Policy Decision making for Future climate change (d4PDF)	RCP8.5	1.5-K, 2-K, and 4-K temperature increases since the industrial revolution	60	20	100

Although NHRCM has been run for these datasets at various resolutions, no reports have compared the reproducibility of NHRCM at different resolutions. Additionally, although the level of global warming depends on regions of Japan, no discussion of the linearity of future changes in temperature, precipitation, and snowfall in Japan with respect to the level of global warming has been reported. The annual maximum snow depth is expected to decrease because of global warming, but the bias correction is necessary, depending on the resolution. However, no correction method that appropriately applies to many locations using a small amount of data has been established. The decrease in snow cover due to global warming can affect the atmosphere by causing roughness and albedo changes through ground surface exposure, but such discussion has been difficult because of the model resolution.

In this study, we address the aforementioned issues. Chapter 2 investigates the reproducibility of the NHRCM simulations at different resolutions and discusses the linearity of climate change around Japan with respect to the level of warming. Chapter 3 presents a method for correcting a small amount of data (only one per year) at multiple locations for future data projection. Chapter 4 discusses the influence of the decrease in snow cover due to global warming on the atmosphere using a high-resolution dataset with a 2-km grid spacing.

Chapter 2. Scalability of future climate changes across Japan examined with large-ensemble simulations at + 1.5 K, +2 K, and + 4 K global warming levels.

2.1 Introduction

The Meteorological Research Institute has been developing a non-hydrostatic regional climate model (NHRCM, Sasaki et al. 2008) to predict the future climate for Japan based on an operational non-hydrostatic model from the Japan Meteorological Agency. We performed high-resolution climate simulations using 5-km grid spacing and using 2-km grid spacing NHRCMs nested from the global model with 20-km grid spacing (Mizuta et al. 2012, Murata et al. 2017). Increasing the resolution of the NHRCM improves the representation of the terrain and leads to the elucidation of detailed physical processes. Murata et al. (2017) showed that the NHRCM better represents the extremes of surface air temperature (SAT) and precipitation by increasing the horizontal resolution from 5 km to 2 km. However, since the high-resolution model integration requires sizable computational resources, it is not easy to conduct large-ensemble simulations for estimations of the uncertainties in the model-simulated variables.

Mizuta et al. (2017) created a climate simulation dataset, called the database for policy decision making for future climate change (d4PDF) using the Meteorological Research Institute atmospheric general circulation model (MRI-AGCM, Mizuta et al. 2012) with 60-km grid spacing and the NHRCM with 20-km grid spacing. The database contains the outputs of large-ensemble experiments over a 5,000-year span under present and future climate conditions; in the latter, the global average SAT is 4 K higher relative to preindustrial levels. Fujita et al. (2019) created a dataset for +2 K conditions as a sub-dataset of the d4PDF for risk assessments of extreme weather events based on the 2K goal of the Paris Agreement. The resolution of the model used for the d4PDF is coarse compared to the experiments using 2-km or 5-km grid spacings, but many model-simulated samples of infrequent phenomena are available thanks to large-ensemble simulations. Kawase et al. (2016) showed that rare and strong snowfall amounts in mountainous areas became stronger under a +4 K climate scenario than under the present climate. Fujita et al. (2019) investigated the future changes of the relationship between extreme hourly precipitation events and daily mean SATs in Japan, and found that hourly precipitation will become stronger for higher-SAT days and slightly weaker for lower-SAT days in the future.

The Paris Agreement aims to pursue efforts to limit the SAT rise to +1.5 K, and to at least keep the global temperature increase below +2 K compared to preindustrial levels. Researchers have been investigating the differences of changes in extreme events and impacts on human society and on ecosystems between the +1.5 K and +2 K warming cases (Masson-Delmotte et al. 2018). In a research project, the HAPPI (half a degree additional warming, projections, prognosis and impacts) multi-model experiments (Mitchell et al. 2016, Mitchell et al. 2017) provided an assessment framework and

a simulation dataset for climates at the +1.5 K and +2 K levels. Liu et al. (2018) showed that a moderation of drought risks appears between the +1.5 K and +2 K levels. Lee et al. (2018) indicated that warming by more than half a degree brings more intense and more frequent precipitation events to the Asian monsoon region. Shiogama et al. (2019) suggested that regions with relatively large increases of extreme hot days, heavy rainfall, high streamflow and labor capacity reductions related to heat stress coincide with those countries that are characterized by low CO2 emissions, low income, and high vulnerability. Limiting global warming to 1.5 K, compared to 2 K, lowers these inequalities.

Most studies of the +1.5 K climate simulation have used global models, but Trentini et al. (2019) and Leduc et al. (2019) used regional climate models for the European and North American domains, respectively. However, there was no regional climate dataset that represented spatially detailed climate states around Japan under the +1.5 K climate scenario.

The purpose of this chapter is to investigate the regional characteristics of the increase rate of surface air temperature and precipitation using the large ensemble past and future climate simulation assuming +1.5 K, +2 K, and +4 K relative to preindustrial period. For this purpose, over a 1,500-year span of ensemble +1.5 K climate simulations with the NHRCM was performed as a subset of the d4PDF. We discuss the linearity of regional climate states for the present, +1.5 K, +2 K, and +4 K climates, that is, scalability. Creating climate model datasets is time and computationally resource intensive, so the level of temperature increase that can be calculated is limited. Scalability studies can provide low-cost estimates of climate change at uncomputed temperature rise levels using limited warming rise level datasets. In addition, we present results which suggests the necessity of additional mitigation measures for the +2 K climate case rather than for the +1.5 K climate case.

2.2 Experimental design

We used the MRI-AGCM with a 60-km grid spacing (Mizuta et al. 2012) and the NHRCM20 with a 20-km grid spacing (Sasaki et al. 2008). Using the MRI-AGCM outputs as boundary conditions, dynamical downscaling was performed with the NHRCM20. The experimental design followed Mizuta et al. (2017) and Fujita et al. (2019), who conducted large-ensemble experiments under the past climate condition (PAST), +2 K (d2), and +4 K (d4) global mean SAT (gSAT) conditions. In this chapter, we conducted experiments for the +1.5 K gSAT case relative to preindustrial levels (d1.5).

One hundred simulations of the present climate experiments had already been conducted for the period from 1951 to 2010 (Mizuta et al. 2017), in which the monthly sea surface temperature observations (COBE-SST2, Hirahara et al. 2014) were prescribed. In each simulation, the atmospheric models were perturbed by different initial conditions and by spatio-temporally varying sea surface temperatures (SST) perturbations. The SST perturbations reflect the observational uncertainties.

In the +1.5 K experiment, we prescribed the SSTs that represent future SST patterns (ΔSSTs) obtained from six models of the Coupled Model Intercomparison Project Phase 5 (CMIP5) plus the

detrended COBE-SST2. The future SST patterns are the differences between the averages for 1991-2010 in the historical experiments and those for 2020-2039 in the Representative Concentration Pathway 8.5 (RCP8.5) scenario experiments. To force the gSATs of the +1.5 K experiment with MRI-AGCM to become +1.5 K, each ΔSST was multiplied by a scaling factor (Table 2.1; Shiogama et al. 2010) which was estimated from the gSAT changes in the CMIP5 experiments (Mizuta et al. 2017). For the greenhouse gas and aerosol concentrations, the values for 2030 in the RCP8.5 scenario were used. Nine ensemble simulations starting from different initial conditions were performed with the aforementioned future SSTs added to the SST perturbations. The integration period of the +1.5 K climate simulations was 29 years, in which the interannual variations of the SSTs are those from 1982 to 2010. The total number of ensembles is 1566 years. Unless otherwise noted, 1450 years are used for analysis of the PAST and 1566 years are used for analysis of the future climate experiments.

Table 2.1. Scaling factors for future SST trend patterns obtained from CMIP5 RCP8.5 runs by six models. The six climate models are CCSM4, GFDL-CM3, HadGEM2-AO, MIROC5, MPI-ESM-MR, and MRI-CGCM. See the Abbreviations section for their full forms.

CCSM4	1.05828
GFDL-CM3	0.638859
HadGEM2-AO	1.17874
MIROC5	1.01876
MPI-ESM-MR	1.09218
MRI-CGCM3	1.22361

2.3 Results and Discussion

2.3.1 Reproducibility of the present climate over the Japanese region

Dynamical downscaling of the NHRCM improves the expressions of topographic effects and the reproduction of extreme phenomena, and maintains the synoptic fields of the MRI-AGCM. Areas of complex mountainous terrain along the center of Japan are more realistically reproduced by the NHRCM20 than by the MRI-AGCM (Fig. 2.1). The distributions of the climatological sea-level pressures (SLP) and the SATs simulated by NHRCM20 under the present climate condition are similar to those of the MRI-AGCM (Fig. 2.2a-b). The precipitation amounts in the mountainous areas of Honshu and on the Sea of Japan side are greater for the NHRCM than for the AGCM because of the realistic expression of topography in the NHRCM. The frequency of daily precipitation events is more realistic in the NHRCM20 than in the MRI-AGCM (Fig. 2.2c). The NHRCM20 has a frequency of daily precipitation that is below 300 mm, close to the observations, and it can reproduce strong daily precipitation amounts greater than 500 mm.

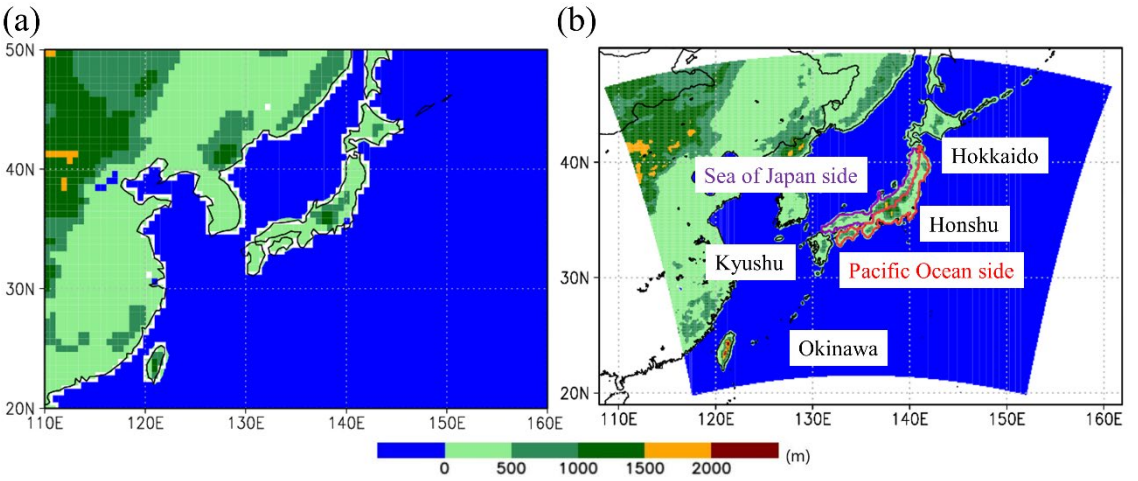

Figure 2.1. Model topographies of (a) MRI-AGCM and (b) NHRCM20. The right panel shows several area names, which are referred to in the text. Red line indicates the Pacific Ocean side in Honshu and purple line indicates the Sea of Japan side in Honshu.

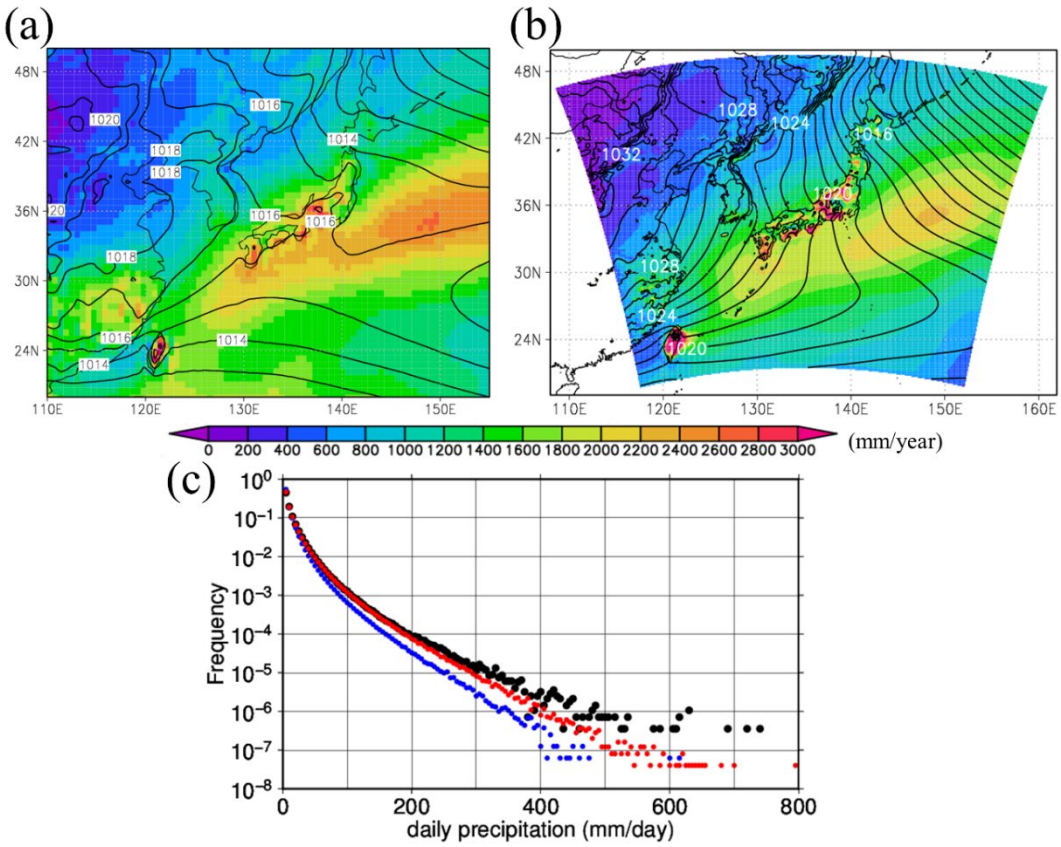

Figure 2.2. Annual accumulated precipitation, SLPs, and frequencies of daily precipitation.
(a) and (b) show annual precipitation (mm; shaded) and annual mean SLP (hPa; contours) by (a) the MRI-AGCM and (b) the NHRCM20. (c) shows the frequencies of daily precipitation for all grids on the Japanese Islands (black: AMeDAS observations, blue: AGCM, and red: NHRCM20).

Figure 2.3a-c shows the scatter plots of the simulated and observed daily surface air temperatures (SAT). Here, the Automated Meteorological Data Acquisition System (AMeDAS) is used as the observation data, and the model grid data closest to the AMeDAS stations are used for comparison. The daily mean SATs (Tmean) agree with the observations so that the model-simulated values are located mostly along the identical line. The bias, root mean square difference (RMSD) and correlation coefficient between the model-simulated and observed Tmean values are 0.48 K, 1.0 K and 0.98, respectively (Table 2.2). The annual minimum SATs (Tmin) values are also reproduced well by the NHRCM20, especially at grid points where the temperatures are greater than −15 ℃, and are distributed mostly along identical lines. Although the annual maximum SATs (Tmax) are distributed near identical lines, the model-simulated temperatures are generally slightly underestimated, and are overestimated at some grid points in those specific areas where the topographic effects are great. The Tmin values of the NHRCM20 are highly biased for observed minimum temperatures below −15℃. This is due to a “no sea-ice condition” in the Okhotsk Sea during the entire simulation, which is a mistake in all experiments of the d4PDF with the NHRCM20. As a result, the Tmin values in eastern Hokkaido are overestimated in the simulations. The simulated Tmax values are biased by -1.2 K compared to the observations (Fig. 2.3b and Table 2.2). This is speculated to be due to the land-cover category definition and the land surface scheme currently adopted in the NHRCM20. This improvement is a future work.

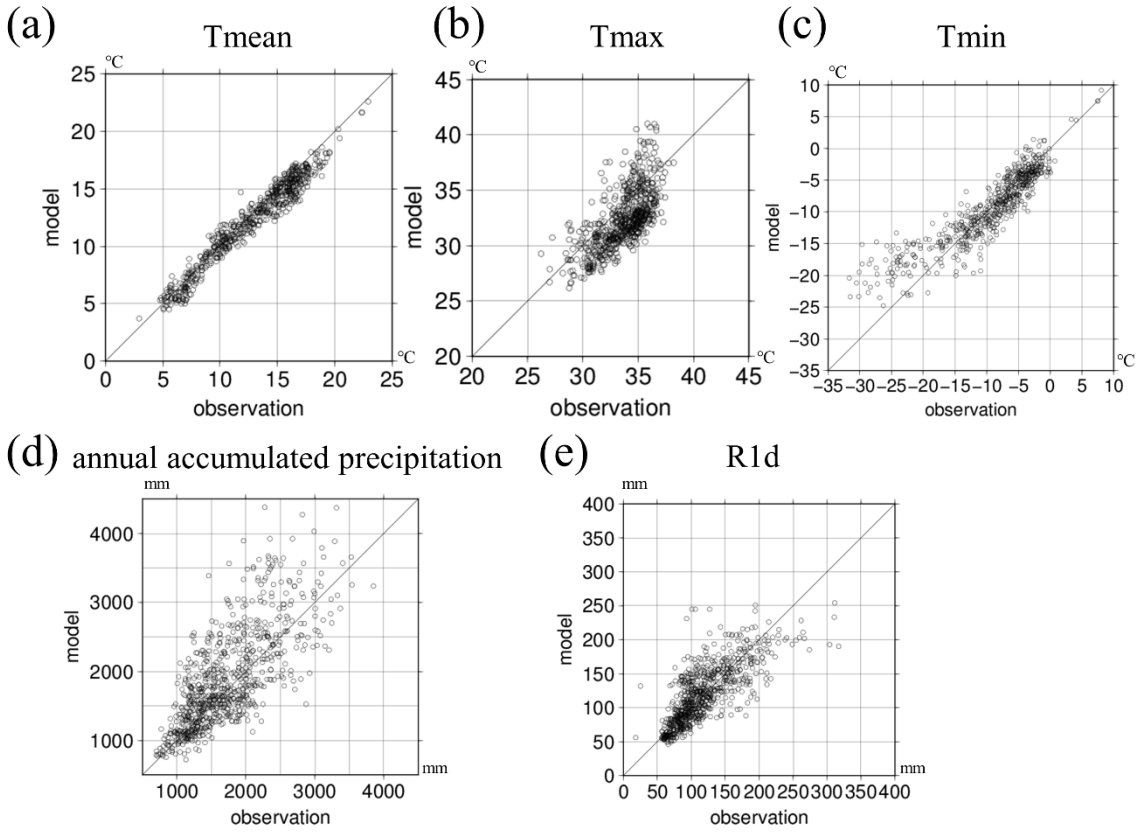

Figure 2.3. Scatter plots of observed vs. model simulated daily temperature and precipitation.
The x and y axes indicate the AMeDAS observations and the model simulations, respectively. In order to match the elevations between the model grid and the AMeDAS, the height correction of the surface air temperature is applied to simulated temperatures using a single lapse rate of 0.0065 Km^{-1} (a: annual mean temperature, b: Tmin, c: Tmax, d: annual precipitation, and e: R1d)

Table 2.2. Biases, RMSDs, and correlation coefficients. Tmean, Tmin, Tmax, annual precipitation, and R1d in NHRCM20, NHRCM05, and NHRCM02 are compared to the AMeDAS observations.

	Bias			RMSE			Correlation coefficient		
Resolution	20 km	5 km	2 km	20 km	5 km	2 km	20 km	5 km	2 km
Tmean	0.48K	-0.38K	0.36K	1.0K	0.66K	0.77K	0.98	0.99	0.99
Tmax	-1.2K	-2.1K	-0.31K	2.5K	2.3K	2.0K	0.69	0.86	0.78
Tmin	0.27K	-1.5K	-1.1K	3.1K	3.4K	2.9K	0.91	0.91	0.93
Annual precipitation	9.0%	11%	1.0%	28%	22%	14%	0.75	0.83	0.91
R1d	1.1%	5.6%	7.8%	25%	21%	22%	0.77	0.87	0.89

Figure 2.3d shows a scatter plot of the annual accumulated precipitations. The annual precipitation is reasonably well reproduced by the NHRCM20 with bias of 9%, an RMSD of 28%, and a correlation coefficient of 0.78. The biases are smaller than the standard deviations of the interannual variations for 60% of all stations. Figure 2.3e shows a scatter plot of the annual maximum daily precipitation (R1d). The annual maximum daily precipitation is well reproduced by the NHRCM20 with slightly better values for the bias, the RMSD, and the correlation coefficients than those of the annual averages. The biases at 90% of all stations are smaller than the standard deviations of the interannual R1d's.

Murata et al. (2017) conducted present-climate simulations with a 5-km-mesh NHRCM (NHRCM05) and with a 2-km-mesh NHRCM using an urban canopy model (NHRCM02) over a 20-year span. The NHRCM20 shows good performance for the daily-scale precipitation and temperatures compared to the NHRCM05 and the NHRCM02, although an increase in the horizontal resolution slightly improves the reproducibility of the SATs and of the precipitation levels due to the effects of topography (Table 2.2). This result is consistent with that of Takayabu and Hibino (2016). We cannot conduct large-ensemble experiments with high-resolution models due to limitations of computational resources. Note that the lateral boundary conditions of the NHRCM05 and the NHRCM02 are the MRI-AGCM, with an approximate 20 km horizontal resolution, which are different from that of the NHRCM20 in the d4PDF dataset. In this sense, the NHRCM20 has an advantage in performing large-ensemble simulations. Note that a great advantage of the 2-km- and 5-km-resolution NHRCMs is the high reproducibility of sub-daily heavy precipitation events required by the assessment studies (Sasaki et al. 2011).

2.3.2 Future changes in SATs

Figure 2.4 shows the future changes in the SATs. The north-south contrasts of SAT warming are seen clearly in d2 and d4. The SAT increases in winter are larger than in summer. In winter, the temperature increases are greater in the mountainous areas of Honshu compared to the surrounding plains. Such features are not seen in summer.

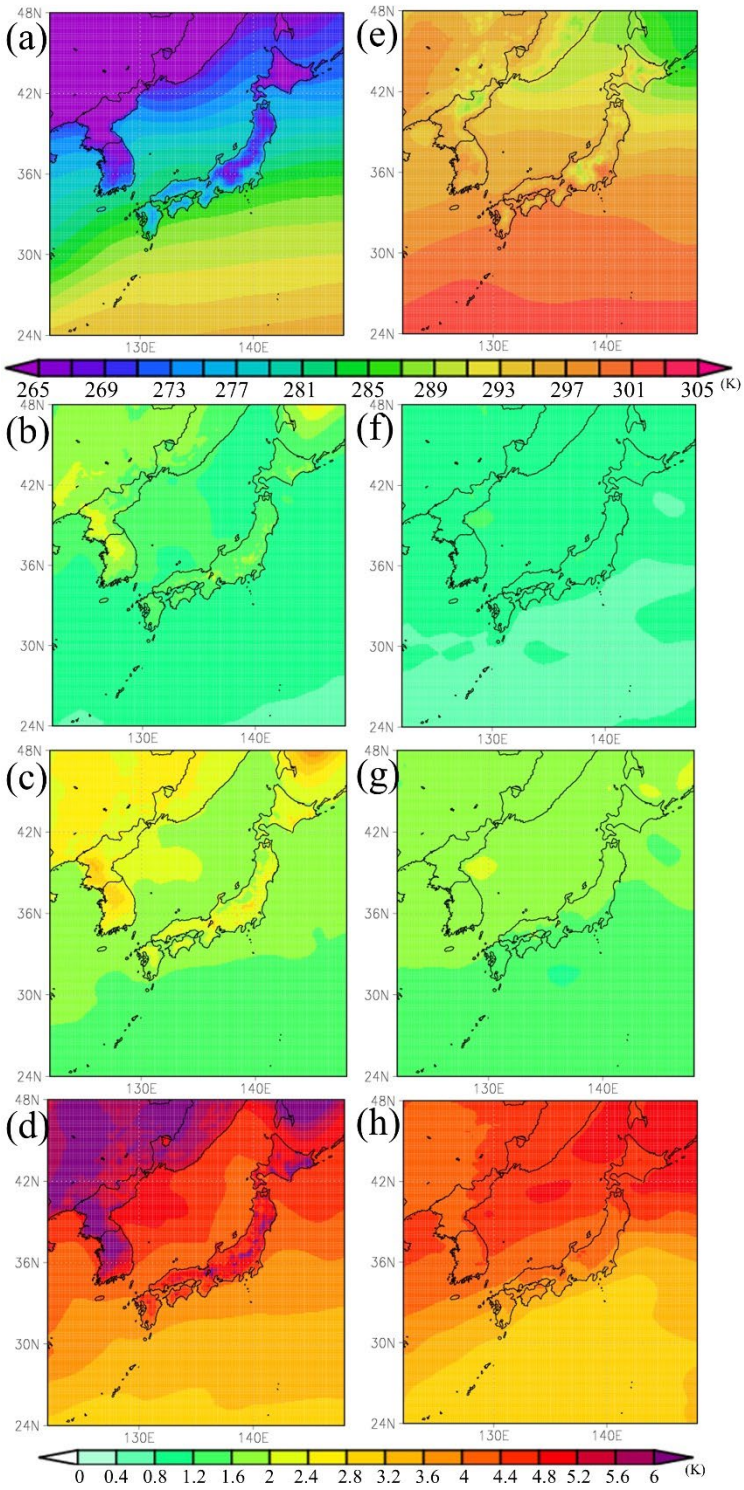

Figure 2.4. Seasonal mean SATs and future SAT changes.

Seasonal mean SATs (K) of PAST (a and e) and the future SAT changes of d1.5 (b and f), d2 (c and g), and d4 (d and h). Values for DJF and JJA are shown in the left and right columns, respectively. The mean values are based on 1450 years for PAST and 1566 years for the future climate.

Figure 2.5 shows the relationships between latitude and SAT increases. As mentioned above, the distributions of the SAT warming over Japan are caused by the ΔSST distributions (Fig. 2.6) and the anthropogenic forcing given in the d4PDF experiments (Mizuta et al. 2017). The meridional gradient for d1.5 is generally zero, while greater warming in the northern region is clear in d2 and in d4. As decreases in snow accelerate SAT increases due to snow-albedo feedback (Matsumura and Sato 2011, Scherrer et al. 2012), future SAT increases appear abnormally large in winter for those grid points covered by snow in PAST. In summer, the relationship between latitude and the SAT increases is clear for d2 and d4 with meridional gradients (±standard deviations) of +0.029 ±0.020 $K^{\circ-1}$, and +0.089 ±0.025 $K^{\circ-1}$, respectively. The change for d1.5 is +0.013 ±0.022 $K^{\circ-1}$ and is considered as insignificant, according to the student's t-test.

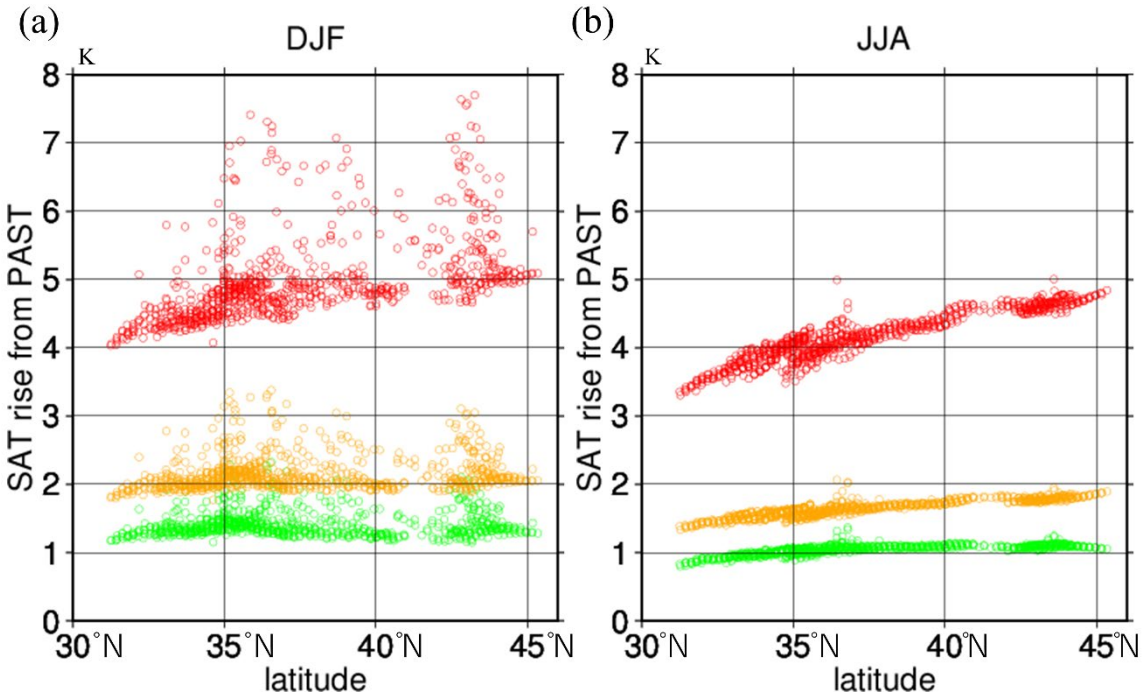

Figure 2.5. Scatter plots of increases in seasonal mean SAT relative to the present climate as a function of latitude.

(a) DJF and (b) JJA. Values at all land grids on the Japanese Islands were used and were based on 1450 years average for PAST and 1566 years average for the future climate. The green, yellow, and red circles indicate d1.5, d2, and d4, respectively.

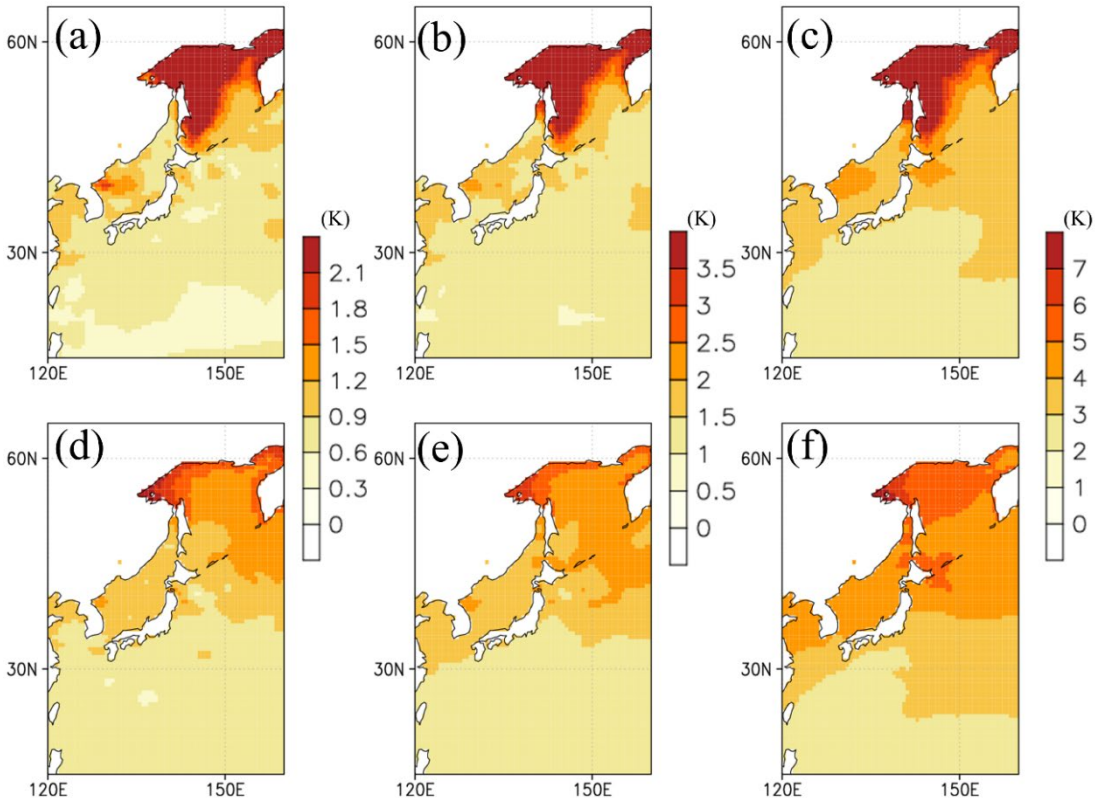

Figure 2.6. The distribution of ΔSST in DJF and JJA averaged for all ensemble members. The first row (a, b, and c) shows the distributions in JJA and second row (d, e, and f) shows the distributions in DJF. The future changes of d1.5, d2, and d4 are presented in the left (a and d), center (b and e), and right (c and f) columns, respectively.

How future SATs change as the gSATs increase is discussed using Fig. 2.7. Here, Tmean, Tmax, and Tmin are the averages for all grid points located over the Japanese Islands. The Tmean increases are 1.2 K, 1.9 K, and 4.6 K for the d1.5, d2, and d4 cases, respectively, relative to those of PAST. Namely, they are approximately linearly 1.3 times larger than the gSAT increases. Therefore, it is concluded that future changes in the Tmean values are generally scalable with respect to global warming levels. Similarly, the Tmax and Tmin increases are scalable with factors of 1.2 and 1.6 to the gSAT, respectively. Due to reductions of snow coverage, the Tmin rate of increase is higher than that of the Tmean. Since the Tmean is approximately average of the Tmax and the Tmin, the increase rate of the Tmean is larger than that of the Tmax. The standard errors of ensemble-mean temperatures are small, and therefore, the future changes in the mean value of the Tmean, Tmax, and Tmin are regarded to be significant. The standard deviations of the Tmean are smaller than that of the Tmax and Tmin. The spreads of the Tmean, Tmax, and Tmin has no apparent response to the gSAT rises. Since the SAT in the Japanese Islands rises linearly, assuming 3 K rise in gSAT, Tmean, Tmax, and Tmin are estimated to be 3.2 K, 2.9 K, and 3.9 K, respectively.

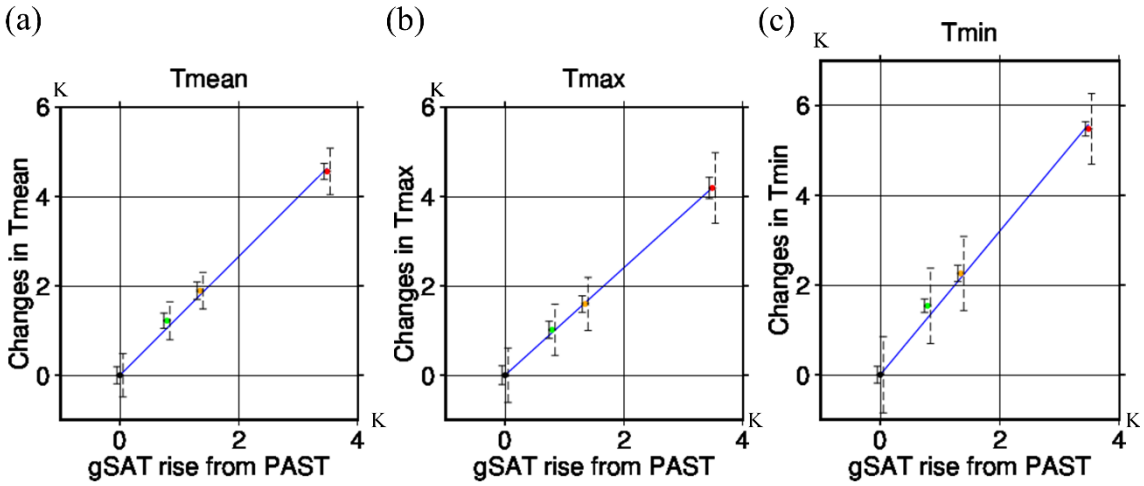

Figure 2.7. Future changes in Tmean, Tmax, and Tmin.

(a)Tmean, (b) Tmax, and (c) Tmin are averaged on all land grids on the Japanese Islands relative to those of PAST as a function of gSAT increases. The bars with solid line indicate standard errors of the ensemble mean and the bars with dashed line indicate standard deviations. Linearly fitted line is shown in each panel. The black, green, yellow, and red circles indicate PAST, d1.5, d2, and d4, respectively.

2.3.3 Future changes in Precipitation

Figure 2.8 shows three-month accumulated precipitation amounts and the average SLP. In winter, d1.5, d2, and d4 all show trend patterns of the changes in the SLP similar to those seen in previous studies (Kimoto 2005, Hori and Ueda 2006, and Kawase et al. 2015): low SLPs in the west and high SLPs in the east. It is thought that the continental SLPs become lower because the temperature increases are greater on the Eurasian continent than for the oceans (Fig. 2.4).

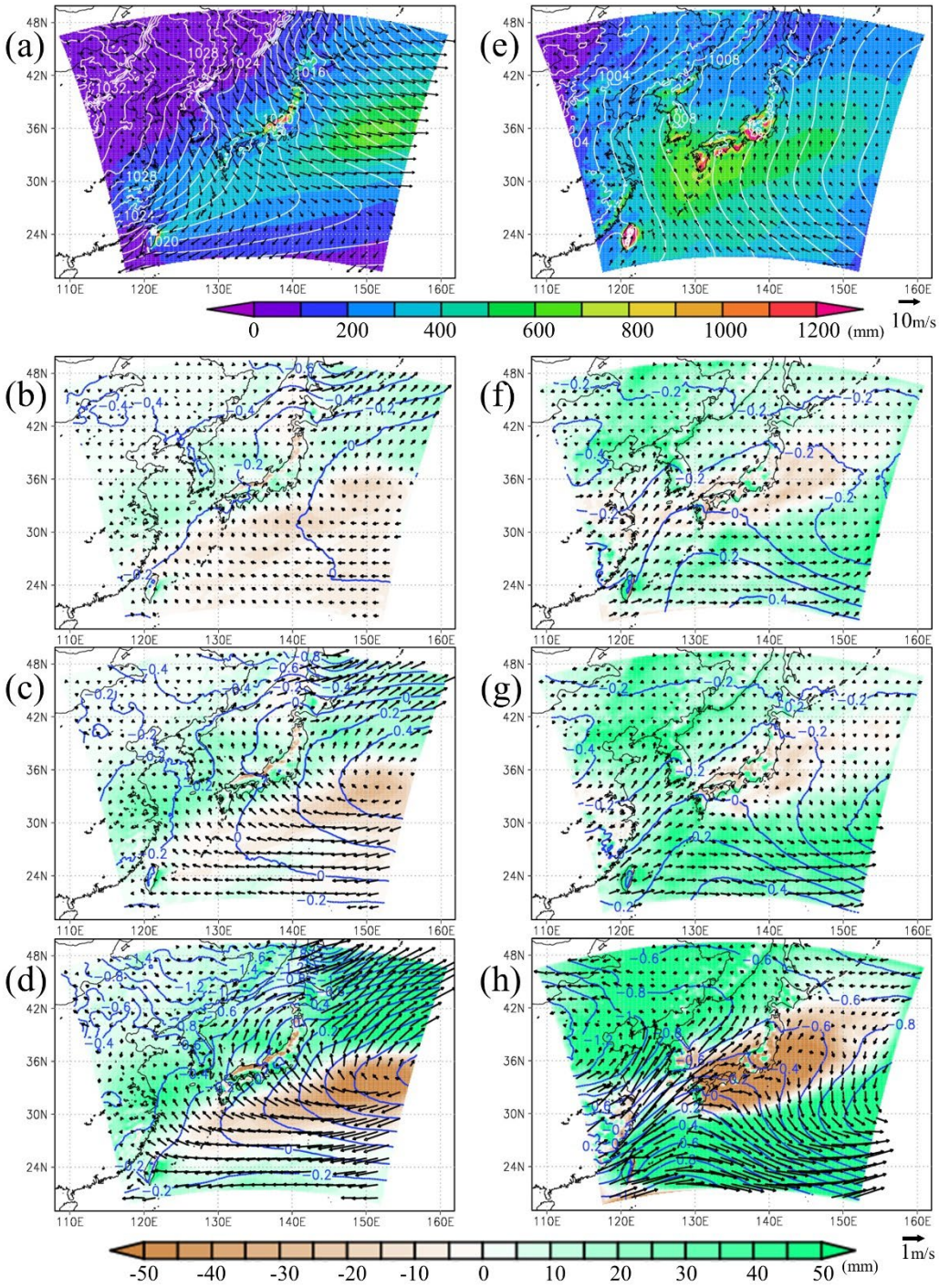

Figure 2.8. Seasonal precipitation amounts, and seasonal average SLPs and wind vectors.
The shading, contours, and vectors denote precipitation amounts (mm), SLPs (hPa), and wind vectors (ms^{-1}), respectively, for (a, b, c, and d) DJF and (e, f, g, and h) JJA. (a) and (e) show the climatologies of PAST and the future changes of (b and f) d1.5, (c and g) d2, and (d and h) d4 are presented.

Commonly, in d1.5, d2, and d4, future summer precipitation levels tend to decrease around Honshu and to increase outside of this area (Fig. 2.8e-h). Winter precipitation tends to increase over the Sea of Japan and to decrease south of the Japanese Islands, while the Sea of Japan side of Honshu shows decreases in winter precipitation (Fig. 2.8a-d). Average precipitation changes for both summer and winter months show a slightly different trend at some locations on land than at sea. On land, precipitation tends to increase in areas on the upwind side of the wind change vector due to changes in topographic convergence caused by changes in the circulation field.

Here, we define the SLP difference between two grid points, (130°E, 37°N) and (140°E, 37°N) as an index of the strength of the characteristic atmospheric SLP distribution in winter, i.e., high SLPs in the west and low SLPs in the east. Large indices are reflected by stronger winter monsoons, and the pattern is opposite to that of the future changes mentioned above. The index is 3.98 hPa in PAST and decreases by 0.16 hPa, 0.26 hPa, and 0.47 hPa in d1.5, d2 and d4, respectively. The changes in the indices are closely scalable with respect to gSAT increases. In summer, the SLPs south of Japan become higher and the SLPs east of Japan become lower in d1.5, d2 and d4 (Fig. 2.8). The subtropical high pressure zone, which covers the Japanese Islands in summer, retreats in the east of Japan and extends to the areas south of Japan in the future climate compared to the present climate. The changes in SLPs in the rectangular region from 27°N to 38°N and from 145°E to 152°E are -0.19, -0.29, and -0.78 hPa in d1.5, d2, and d4, respectively, and these are mostly scalable. Those in the area from 24°N to 26°N and from 125°E to 135°E are also scalable: +0.25, +0.31, and +0.70 hPa for d1.5, d2, and d4, respectively. In summary, the SLP changes in winter and summer appear as scalable changes to global warming.

Table 2.3 shows the correlation coefficient patterns of precipitation changes in the Japanese Islands. The correlation coefficients for the changes in annual and seasonal average precipitation amounts between future climate experiments are very high. This indicates that the changes in precipitation amounts appear similarly regardless of the temperature increase, thus responding to the future SST trend patterns prescribed. In JJA, the changes in precipitation amounts are highly correlated between d1.5 and d2. In contrast, there are lower correlation coefficients between d1.5 and d4 and between d2 and d4 than for the other cases. As presented later, these are unlikely to respond simply to future SLP changes (Fig. 2.8).

Table 2.3. Pattern correlation coefficients of future changes in precipitation amounts. The values are the pattern correlation coefficients of future changes in annual and seasonal precipitation amounts for all grid points in the Japanese Islands between two selected levels of warming.

	d1.5 vs d2	d1.5 vs d4	d2 vs d4
ANNUAL	0.94	0.88	0.94
DJF	0.96	0.92	0.96
MAM	0.94	0.95	0.95
JJA	0.91	0.59	0.64
SON	0.90	0.95	0.89

One of the characteristics of the Japanese climate is the seasonal contrast of precipitation events on the Sea of Japan side and on the Pacific Ocean side, which are separated by the central mountains. Figure 2.9 shows the future changes of precipitation amounts on the two sides of Honshu.

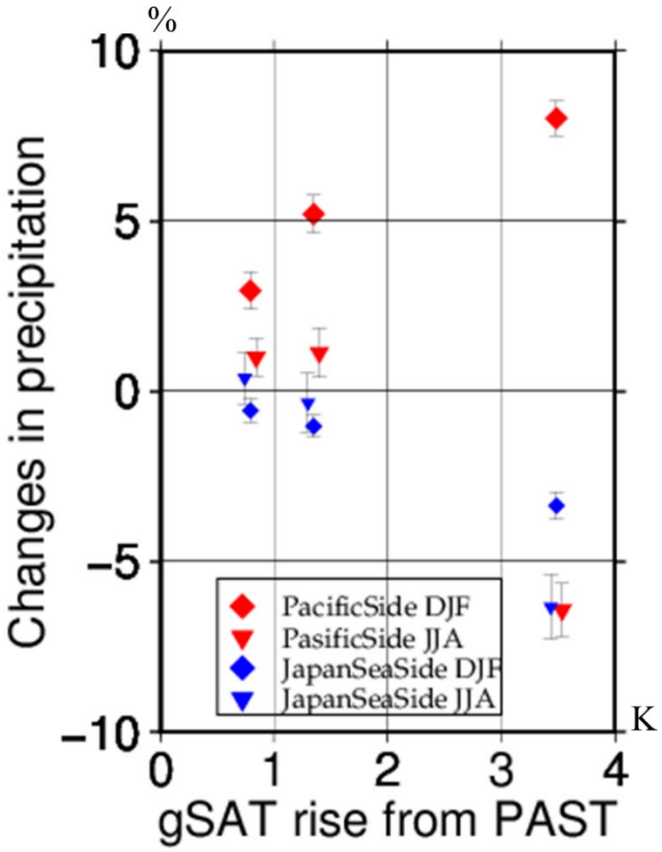

Figure 2.9. Future changes (%) in seasonal precipitation amounts separately for the Pacific area side and the Japan Sea side areas in Honshu.

The red and blue colors indicate the Pacific side and the Japan Sea side, respectively. The squares and triangles indicate DJF and JJA, respectively. The error bars denote the standard errors of the ensemble mean.

In winter, dry climate states generally appear on the Pacific Ocean side in the present climate conditions, but the precipitation amounts increase in the future (red squares in Fig. 2.9). By contrast, precipitation events, including snowfall, decrease on the Sea of Japan side (blue squares). These future tendencies are statistically significant and scalable. The possible reasons are as follows. Because the southeasterly winds from the Pacific Ocean to the Japanese Islands become stronger due to future changes in the circulation field in winter, precipitation amounts increase in the areas on the Pacific side, located on the windward side of the mountains. Conversely, precipitation decreases on the Sea of Japan side, where the northwesterly winds from the Sea of Japan become weaker.

On the other hand, in summer, there is a large jump between d4 and the other cases. The areas of Honshu with reduced precipitation become wider in d4 than in the other two experiments. Concurrently, in d4, the subtropical high around Okinawa is stronger than in d1.5 and d2, and extends to around Kyushu (Fig. 2.8f-h) and weakens east of Japan. As a result, the surface wind changes show divergence around Honshu due to both the strengthening of the southwesterly winds on the Sea of Japan side and the strengthening of northerly winds on the Pacific Ocean side. Therefore, summer precipitation amounts decrease on both the Sea of Japan side and on the Pacific side in Honshu (Fig. 2.9). However, Ose (2019) pointed out that future changes in summer precipitation around Japan are highly uncertain although the decrease in summer precipitation around Japan is predicted by several models.

Although future precipitation changes vary depending on seasons and regions, the annual precipitation amounts in Japan have no clear relationship with gSAT increases (Figure 2.10a). The future precipitation changes of d4 seen largely in Fig. 8 are mostly cancelled out. The future annual precipitation amounts appear to significantly increase in the future climate simulations by approximately 0.8%. Whereas the increases in mean value of annual precipitation due to moisture increase with the gSAT rises are canceled out by changes in circulation fields, the standard deviations of annual precipitation become large because of the moisture increase (Pendergrass et al. 2017). The future R1d values increase approximately linearly with the global warming levels (Figure 2.10b), and the increase rates are $7\%K^{-1}$, $6\%\ K^{-1}$, and $5\%\ K^{-1}$ at d1.5, d2, and d4 respectively. These values agree with the theoretical values from the Clausius-Clapeyron (CC) relationship of $6\%K^{-1}$ to $7\%K^{-1}$ for strong precipitation (e.g., Wang et al. 2017, Gao et al. 2018). The increase rates of R1d become slightly smaller as the gSAT rises due to the development of the divergence fields in summer (Fig. 2.8). The standard errors of ensemble-mean R1d indicate that the increase of R1d due to global warming is regarded to be significant. The standard deviations of R1d become large as the gSAT rises and this result is caused by moisture increases and occurrence frequency increases in intense tropical cyclones in the future climate (Yoshida et al. 2017, Kitoh and Endo 2019).

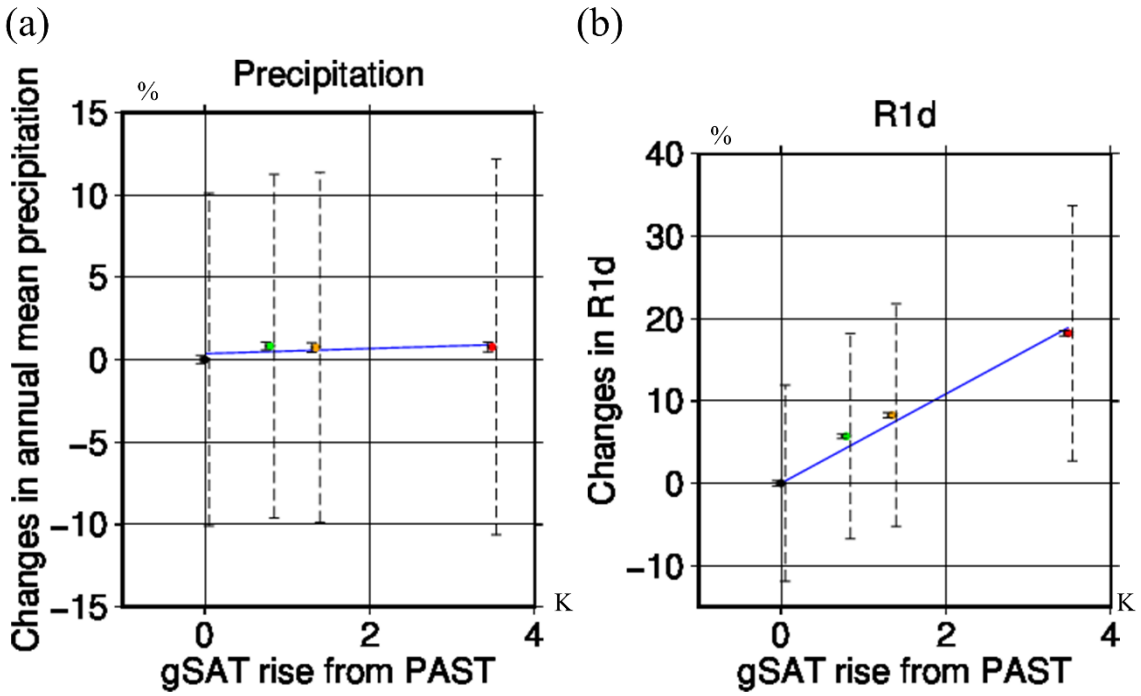

Figure 2.10. Changes in annual mean precipitation and R1d.

Changes in (a) annual mean precipitation relative to the gSAT increases and in (b) R1d relative to the gSAT increases. Values are averaged on all land grids on the Japanese Islands. The solid bars indicate standard errors of the ensemble mean and the dashed bars indicate standard deviations. The blue color denotes linear fitting. The black circle, green circle, yellow circle, and red circle indicate PAST, d1.5, d2, and d4, respectively.

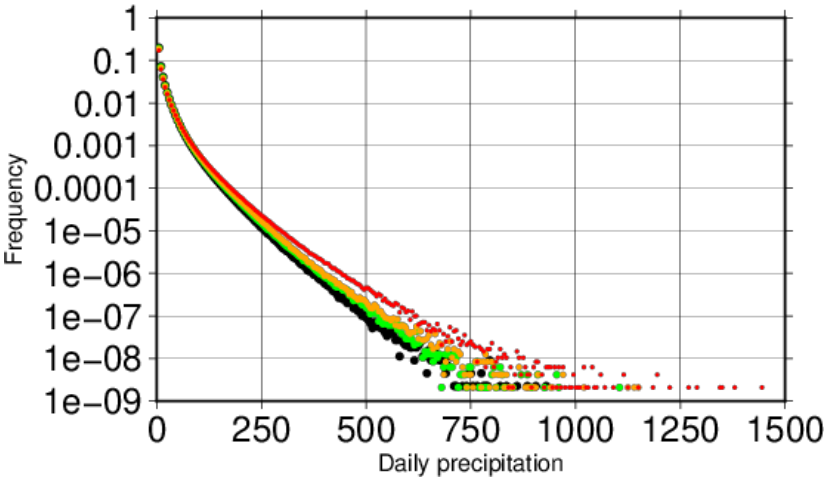

Figure 2.11. The probability density function of daily precipitation. The black circle, green circle, yellow circle, and red circle indicate PAST, d1.5, d2, and d4, respectively.

Although the intensity of heavy precipitation has become stronger due to global warming, the annual precipitation around Japan has leveled off. One of the reasons for the leveling off the annual precipitation is that the frequency distribution of precipitation intensity is changing due to global warming. The figure 2.11 shows the frequency distribution of precipitation intensity for each level of global warming, showing that the ratio of days with heavy precipitation of over 200 mm per day increases as the level of global warming increases. On the other hand, the percentage of days with no precipitation increases from 59% in the present climate to 60%, 61%, and 63% in 1.5K, 2K, and 4K climates, respectively, indicating that annual precipitation remains unchanged. Although the amount of water vapor in the air increases due to global warming, the amount of saturated water vapor also increases, making it harder for clouds to form. As a result, the number of days without precipitation will increase and heavy rainfall will be enhanced (Giorgi et al. 2011; Trenberth, 2011).

One of the factors contributing to the variability in the future trends of accumulated precipitation is the influence of the future change pattern of SSTs, which has a significant impact on the future prediction and may cause different changes in the circulation field. The Figure 2.12 and Figure 2.13 show the mean pressure and accumulated precipitation in winter and summer for each of the six SSTs, showing that each SST has a different trend. In other words, the pattern of the future change in seasonal precipitation amount is highly dependent on SSTs. On the other hand, R1d tends to increase with warming regardless of which SST is selected. As shown in the Figure 2.14, R1d becomes larger at most locations in the domain, and precipitation increases linearly with global warming regardless of which SST is selected. This result is consistent with the results of Salathé et al. (2010).

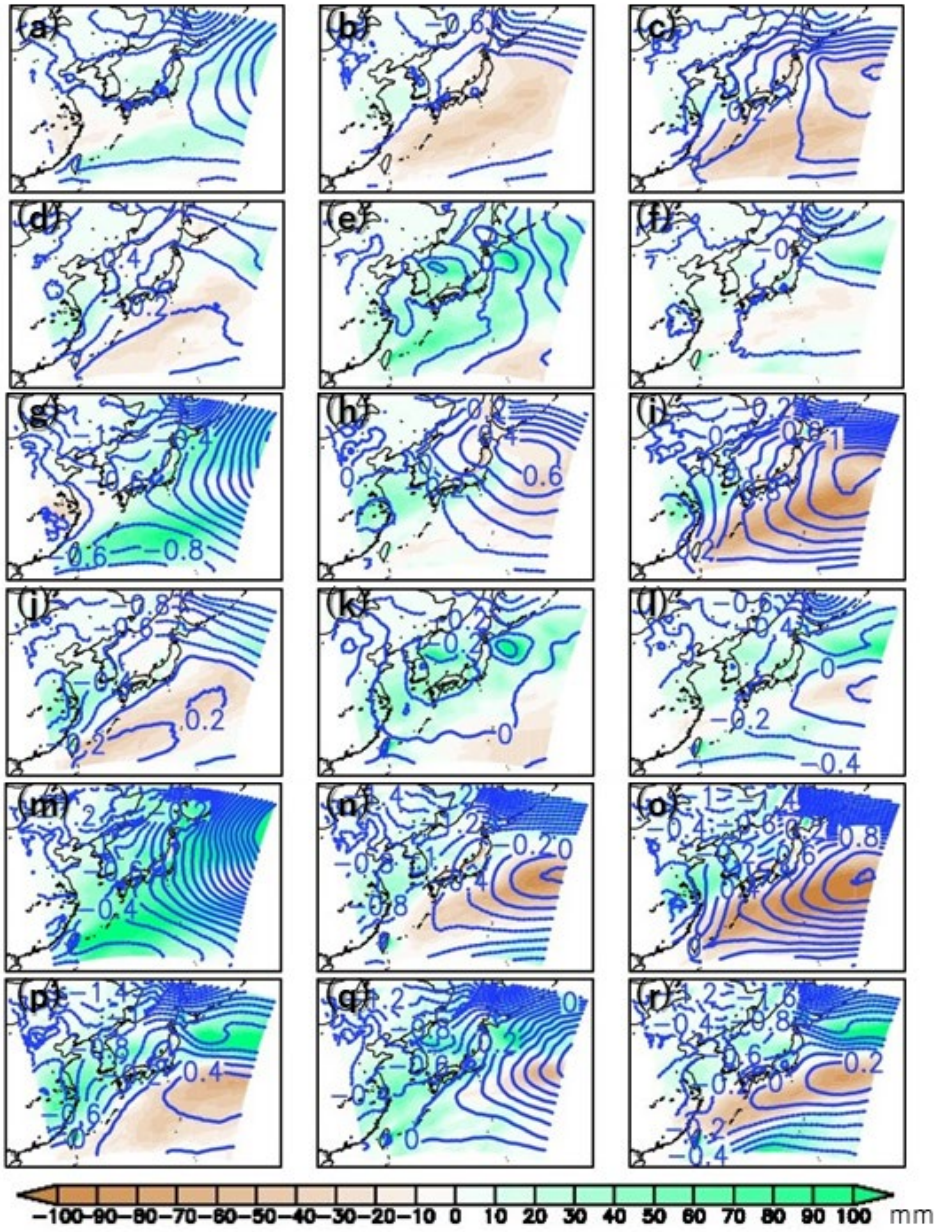

Fig. 2.12 Future changes in winter precipitation (shade, mm) and winter mean SLP (contours, hPa) are shown, and (a)-(f) indicate future changes in d1.5 with SSTs of MI, CC, HA, MR, MP, and GF, respectively. (g)-(l) and (m)-(r) show those of d2 and d4, respectively.

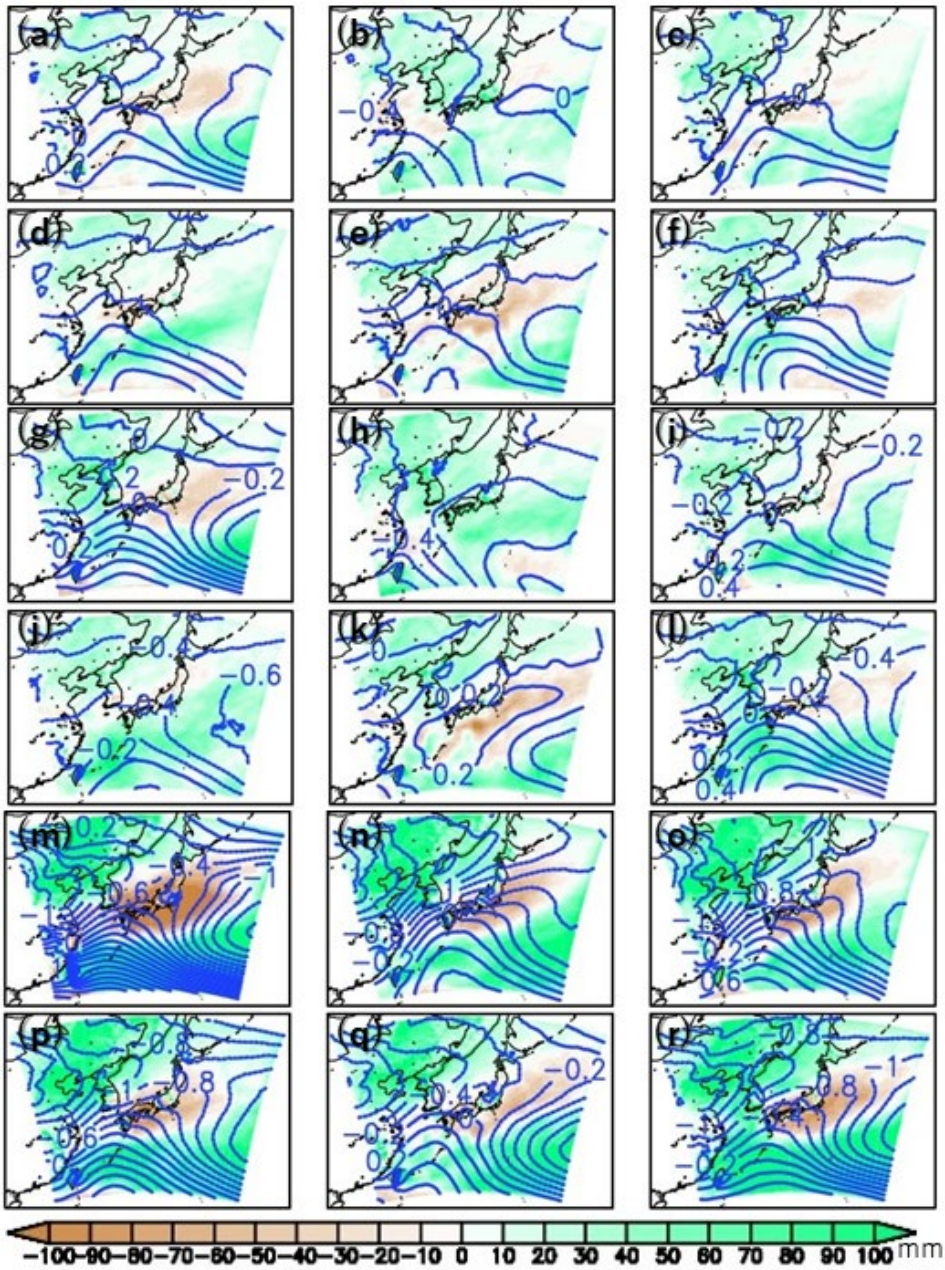

Fig. 2.13 Future changes in summer precipitation (shade, mm) and summer mean SLP (contours, hPa) are shown, and (a)-(f) indicate future changes in d1.5 with SSTs of MI, CC, HA, MR, MP, and GF, respectively. (g)-(l) and (m)-(r) show those of d2 and d4, respectively.

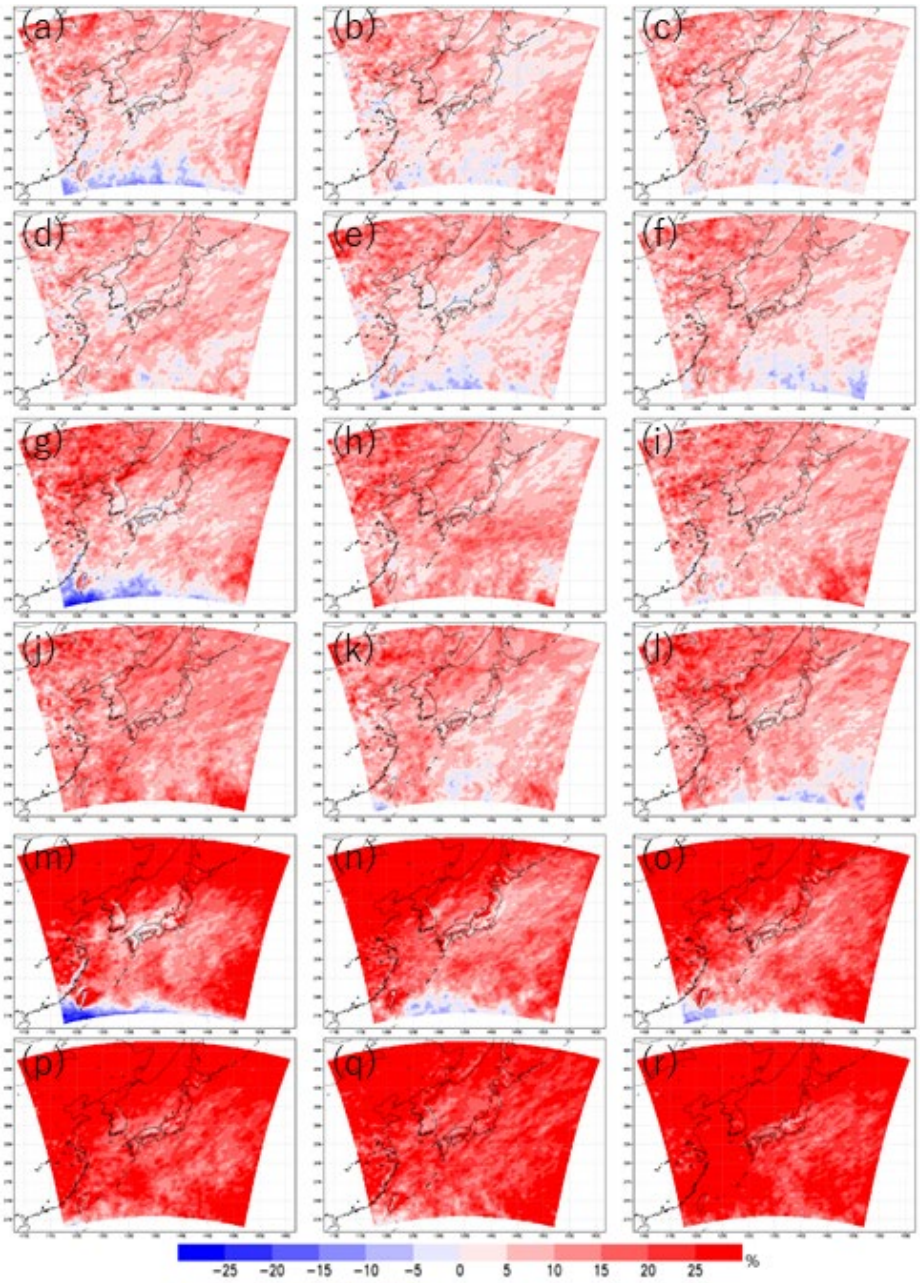

Figure 2.14. Future changes in R1d are shown, and (a)-(f) indicate future changes in d1.5 with SSTs of MI, CC, HA, MR, MP, and GF, respectively. (g)-(l) and (m)-(r) show those of d2 and d4, respectively.

2.3.4 Future changes in snow cover distribution

The Figure 2.15 shows the future change in the number of days with snow cover over 1 cm. The number of days of snow cover decreased with increasing temperature, and the change was not linear; the decrease accelerated as the temperature increased. As the snow-covered days decrease, the albedo becomes higher due to the exposure of the ground surface, and the local temperature increase may accelerate, which may lead to a more accelerated decrease in the number of snow-covered days at the grids where the snow-covered days has decreased.

Kawase et al. (2016) showed that for a 4K increase, total winter snowfall in inland Japan would decrease significantly, but heavy once-in-a-decade snowfall would increase, which is attributed to an increase in water vapor supply from the ocean and an enhancement of the Japan Sea polar air mass convergence zone.

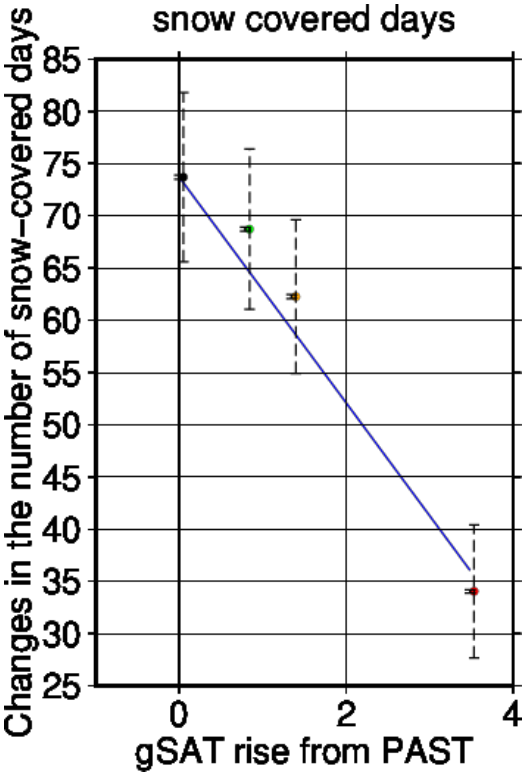

Figure 2.15 Changes in the number of snow-covered days.

The number of snow-covered days is averaged on all land grids on the Japanese Islands as a function of gSAT increases. The bars with solid line indicate standard errors of the ensemble mean and the bars with dashed line indicate standard deviations. Linearly fitted line is shown. The black, green, yellow, and red circles indicate PAST, d1.5, d2, and d4, respectively.

2.3.5 Impacts of a 0.5 degree increase on regional climates

By implementing additional mitigation measures which limit the gSAT rise by +1.5 K, it is

expected that the Tmean increases over Japan would be reduced by 0.7 K (Fig. 2.6) compared to those of the present climate. As shown in Fig. 5, the north-south contrast in SAT increases is small in d1.5, while it becomes larger in d2 and d4. The impact of a 0.5 K rises from d1.5 in the gSAT on the summer temperatures in Japan is 0.85 K in the north and 0.51 K in the south. Similarly, the R1d precipitation amounts over the Japanese Islands increase significantly between +1.5 K and +2 K (Fig. 2.10). Changes in the circulation fields cause a significant increase in winter precipitation on the Pacific side of 2.5% (Figure 2.9), while the winter precipitation amounts on the Sea of Japan side do not exhibit a significant difference between +1.5 K and +2 K.

The increase in R1d due to gSAT rise of 0.5 K is about 4.0%K-1 on average for all land grids on the Japanese Islands, which is smaller than the theoretical value of $6\%K^{-1}$ to $7\%K^{-1}$. There are regional characteristics in the differences in R1d, and it is small at latitudes from 34°N to 41°N (Figure 2.16). The differences of R1d in Hokkaido, located north of 41°N, are larger than other regions due to larger increases in the SATs and close to the theoretical value (Table 2.4). In Kyushu, located south of 34°N, the increase rate of R1d, within the standard error range, does not deviate from the theoretical value. In contrast, the increase rate of R1d in Honshu is significantly smaller than the theoretical value, because the divergence tendency with the progression of global warming prevent increase in R1d (Fig. 2.8).

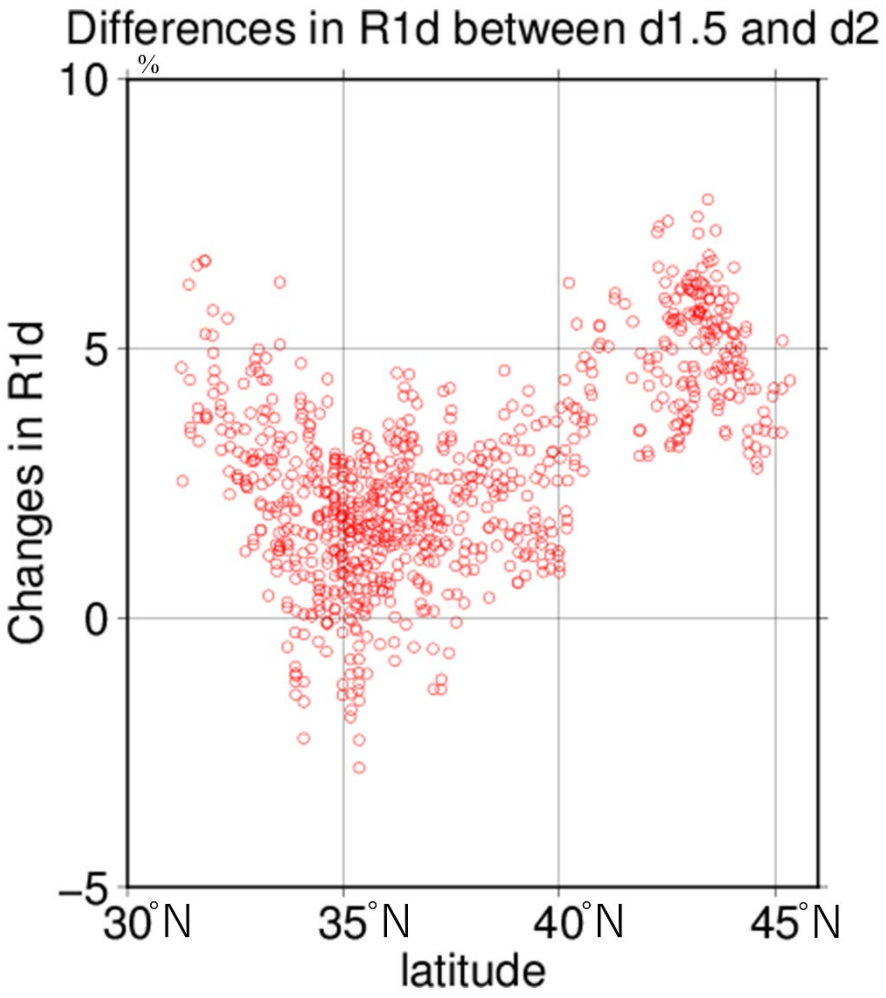

Figure 2.16. Differences in R1d (%) between d1.5 and d2 on land grids in the Japanese Islands.

Table 2.4. Differences in R1d (dR1d) and SAT (dSAT) between d1.5 and d2 with standard errors of the ensemble mean. The right column shows the increase rate of the R1d per 1K (dR1d/dSAT). All land grids in the Japanese Islands are used for ALL.

	dR1d(%)	dSAT(K)	dR1d/dSAT(%K^{-1})
ALL	2.7 ± 0.4	0.67 ± 0.28	4.0 ± 1.1
Hokkaido	5.0 ± 0.8	0.74 ± 0.26	6.8 ± 1.3
Kyushu	3.3 ± 0.8	0.62 ± 0.26	5.3 ± 1.1
Honshu	2.0 ± 0.5	0.65 ± 0.27	3.1 ± 0.5

2.4 Conclusions

In this chapter, we confirmed the reproducibility seen in the regional climate model outputs of the d4PDF, and investigated the scalability of future changes in SATs, SLPs, and precipitation amounts.

The present climate reproducibility of the regional climate model in the d4PDF was confirmed, and it was found that the NHRCM20 performs reasonably comparably to the higher-resolution models for SATs and precipitation at daily time scales.

As a subset of the d4PDF, future climate simulations of the +1.5 K gSATs were performed. The scalability, that is, the linearity of future changes with gSAT increases, was examined by comparing with the PAST, d2, d4 (already available) cases. The future SAT changes in Japan showed a scalable relationship with respect to the gSAT increases for faster rates of warming than that of the gSAT. The meridional warming contrast of the SATs is enhanced as global warming becomes severe. In winter, the zonal SLP differences over Japan decrease, while in summer, the SLPs increase (decrease) south (east) of Japan. These future SLP changes in winter and summer are scalable and weaken the seasonal monsoons. The average precipitation amounts are mostly unchanged regardless of the gSAT increases. Winter precipitation amounts on the Pacific side of the Japanese Islands increase linearly with gSAT increases, while those on the Sea of Japan side decrease linearly. The changes of summer precipitation are not scalable because the areal expansion of the divergence of surface winds around Japan reduces precipitation. Future changes in heavy daily precipitation amounts are scalable to gSAT increases, showing rates of 5-7%K^{-1}. If the gSAT increase is reduced from +2 K to +1.5 K by implementing mitigation measures, the Tmean rise in Japan would be reduced by 0.7 K. Heavy precipitation would also be decreased by 2.7% over the Japanese Island. The increase rate of heavy precipitation has regional characteristics. In Hokkaido, where the SAT warming is the greatest in Japan, the increase rate is larger than other regions, and in Honshu, where SLP have divergent tendency under the global warming conditions, the increase rate is smaller than other regions.

The pattern correlation of precipitation change is high except for the summer season of d4, but there are SSTs with different trends of precipitation change. In this chapter, the weights of each SST were the same, and the differences in the averages were discussed. However, since the effects of the differences in SSTs are significant, it will be important to discuss the certainty of future changes and to consider future projections for Japan with the weights of each SST.

Downscale experiments with fine-resolution models are useful for discussing detailed terrain effects on future climate states. To deal with a wide range of uncertainties in future predictions, ensemble experiments using various regional climate models and ocean-coupled simulations are required. In addition, performing experiments using different levels of global warming will help to elucidate those phenomena that are not scalable. All of these will be future works.

It is difficult to evaluate snow cover with a 20 km resolution model because of its low topographic repeatability. In order to predict the future snow cover, data sets with higher resolution models with better topographic reproducibility are needed.

Chapter 3. Bias Correction of Snow Depth by using Regional Frequency Analysis in the Non-Hydrostatic Regional Climate Model around Japan

3.1 Introduction

Reduction of snow depth is one of the concerns associated with future global warming, because snow is a water resource. In addition, a reduction of snow depth is likely to affect the tourism industry and the ecosystem. Moreover, reduction of snow cover makes albedo smaller and brings about positive feedback. Thus, many researchers have tried to predict snow more accurately in future climate by using regional climate models (e.g., Giorgi et al. 2004; Piazza et al. 2014). The prediction of snow depth is very difficult because snow depth is influenced by many meteorological elements, including precipitation, temperature, and wind. Kurihara et al. (2005) used a regional climate model to project the fine structure of future climate change due to global warming around Japan. However, they could not project changes in snow depth because the land surface scheme of their model did not include processes that could be used to predict snow depth. Sasaki et al. (2008) have shown that the Non-Hydrostatic Regional Climate Model (NHRCM) nested in JRA-25 (Onogi et al. 2007) very accurately reproduced the present climate. Using the Meteorological Research Institute of Japan Meteorological Agency Simple Biosphere (MRI-JMASiB) model (Hirai and Oh'izumi 2004), NHRCM was able to simulate snow depth over Japan. Sasaki et al. (2011) have indicated that the NHRCM nested in the Meteorological Research Institute Atmospheric General Circulation Model (MRI-AGCM) reproduces well the present climate around Japan, although this model underestimates the maximum snow depth on the Japan Sea side of northern Japan. Kawase et al. (2020a) used a 1-km resolution model and showed that warming in higher elevation regions of Japan would result in less snowfall in less snowy years and more intense snowfall in snowier years. Kawase et al. (2020b) used RCP2.6 and RCP8.5, they showed that snowfall decreases under RCP2.6 for most regions except Hokkaido, but increases in Hokkaido even under the RCP8.5 scenario with a large temperature increase.

Sasaki et al. (2012) have projected the future change of maximum snow depth due to global warming, but their model makes no bias correction in its prediction of snow depth. Therefore, there is a high possibility that the projection includes large systematic errors. Sasaki et al. (2013) have projected maximum snow depths in Hokkaido with a bias correction by applying the regional frequency analysis (RFA) introduced by Hosking and Wallis (1997). They indicated that the use of this method substantially improved the reproducibility of snow depth. Before implementing this bias correction method, the observation sites in the projection area must be classified into regions within which climate is relatively homogeneous. The classification process used by Sasaki et al. (2013) requires a trial-and-error step, which is not suited for automatic computer analysis. In this chapter, we developed a new bias correction method that is highly accurate and automatically classifies observation sites. Using the new bias correction method, we projected maximum snow depth in all of

Japan.

We explain the experimental design and reproducibility of the NHRCM in Section 3.2, the methodology of the bias correction in Section 3.3, and the results of the bias correction in Section 3.4. We summarize our findings and offer some concluding remarks in Section 3.5.

3.2 Experimental design and reproducibility of the NHRCM

In this chapter, we analyzed the data produced by Murata et al. (2015), which were calculated by using NHRCM with a 5-km grid spacing. There are 527 x 804 grid points horizontally and 50 layers vertically. This model used fully compressible equations with a map factor and semi-implicit time integration scheme. We used bulk-type cloud microphysics that was based on Lin et al. (1983), Murakami (1990), and Murakami et al. (1994). The Mellor-Yamada-Nakanishi-Niino Level 3 scheme was used for a planetary boundary scheme. Kain-Fritsch scheme was used for the convective parameterization. MRI-JMASiB was used for the biosphere process to calculate snow depth and surface temperature. NHRCM was nested in the MRI-AGCM with a 20-km grid spacing (Mizuta et al. 2012) to simulate the present (1980–1999) and future (2076–2095) climate around Japan. For the future climate, the Representative Concentration Pathways 8.5 scenario was used to project greenhouse gas concentrations. The SST used in this NHRCM dataset is averaged over the SST data calculated by 28 atmosphere-ocean coupled general circulation models (CGCMs) in the Coupled Model Intercomparison Project phase 5 (CMIP5).

Snow depths in Japan are recorded at more than 300 Automated Meteorological Data Acquisition System (AMeDAS) sites. We used AMeDAS sites where the data record was longer than five years for verification of snow depths simulated by the NHRCM. The biases of annual maximum snow depths reproduced by the NHRCM in the present climate are shown in Fig. 3.1. The reproducibility of snow depths on the Japan Sea side of Japan was extremely good, but snow depths in mountainous areas and on the Pacific Ocean side of Japan were overestimated. The reason for this bias is that the coarse resolution does not reproduce the small-scale convection over the Japanese Sea, and the lack of rainfall over the sea results in more precipitation in the mountainous areas (Kawase et al. 2019). The Root Mean Square Error (RMSE) of annual maximum snow depth averaged over all AMeDAS sites in Japan was 50 cm. This RMSE is too large for accurate projection of future changes in snow depth. The bias correction method proposed by Sasaki et al. (2013) is able to correct accurately the simulated snow depths. However, that method is not well suited for computer system applications, because it requires a subjective judgment in the classification process. Therefore, this paper examines a new method for correcting snow depth bias.

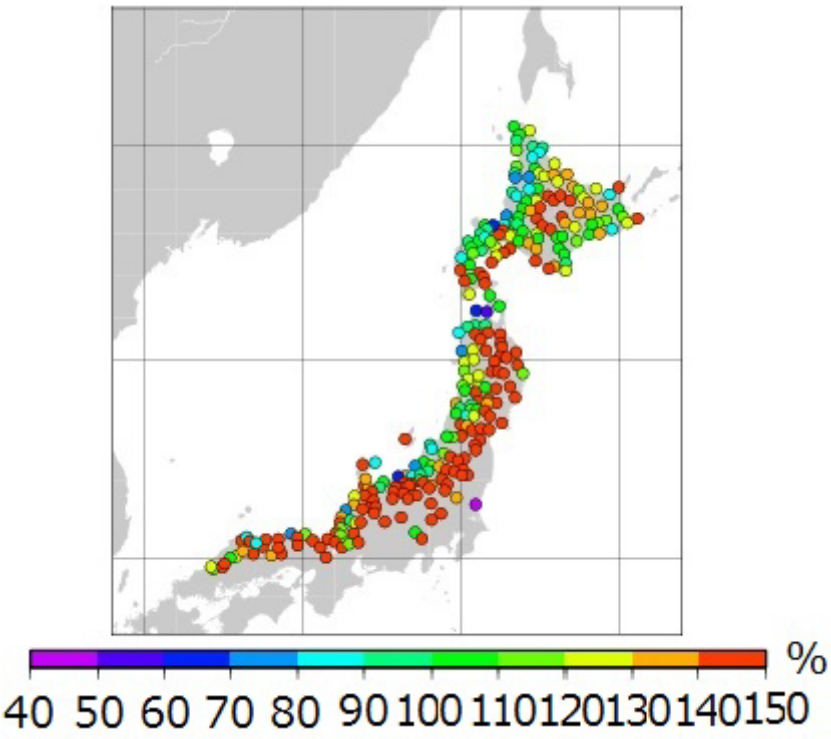

Figure 3.1. Bias of maximum snow depth in the present climate without using bias correction expressed as (simulated/observed) × 100.

3.3 Methodology of bias correction

First, Japan is classified into nine regions, as shown in Fig. 3.2. Cumulative distribution functions (CDFs) of annual maximum snow depth are then generated for each region for both the observation, using data at all AMeDAS sites within each region, and the NHRCM model output for the present climate. Next, the non-exceedance probability value in the NHRCM distribution is used to determine the corresponding quantile value of the non-exceedance probability value in the distribution of the AMeDAS snow depths. This quantile value is used for the bias correction. To obtain CDFs, we use non-exceedance probabilities and quantile values following the method described in Sasaki et al. (2013).

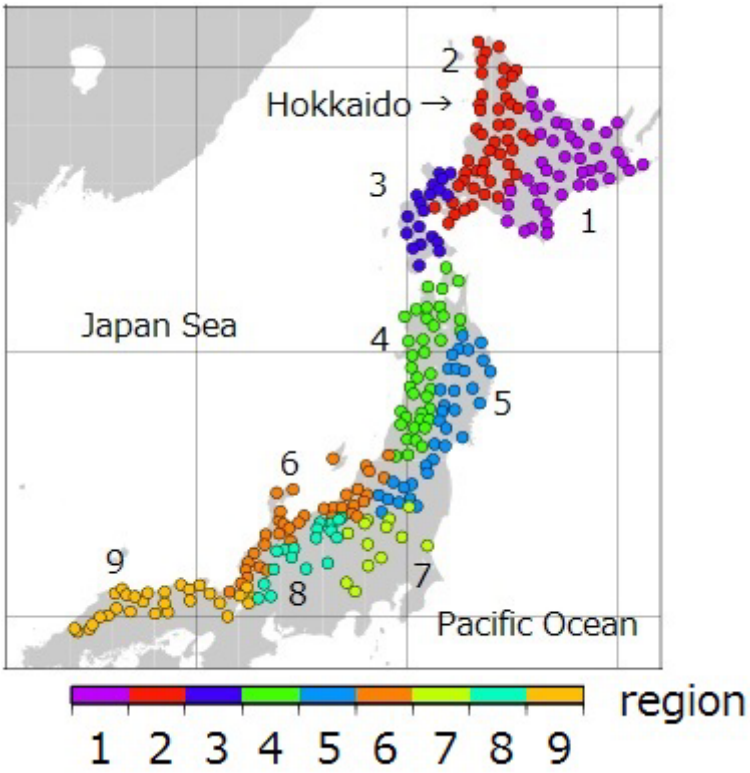

Fig. 3.2. Group areas divided into regions. (1) East Hokkaido (REH). (2) Central Hokkaido (RCH). (3) West Hokkaido (RWH). (4) West Tohoku (RWT). (5) East Tohoku (RET). (6) Hokuriku (RHO). (7) Kanto (RKN). (8) Nagano and Gifu (RNG). (9) Kinki and Tyugoku (RKT).

The maximum snow depths in the future climate are adjusted based on the difference of the fitted curves for CDFs between the observed and simulated depths in the present climate. Because the approximate functions do not always fit the sample data, corrected values are occasionally worse than the original. In the case that non-exceedance probability values are too large, corrected values in the future are sometimes negative, so these values are fixed at 0 in our method. This can give bias corrected data artificial characteristics. The final adjusted maximum snow depth in the future, SD_{fca}, is calculated at each site using the following equation:

$$\overline{SD_{fca}} = \overline{SD_o} \times \overline{SD_{fc}}/\overline{SD_{pc}}, \quad \cdots \quad (3.1)$$

where $\overline{SD}$ is maximum snow depth averaged over all years, and the suffixes o, f, p, and c indicate observation, future, present, and corrected value, respectively. By using $\overline{SD_{fca}}$, the change in the bias corrected future snow depth is more natural. Hereafter, this method is called final correction for future snow depths (FTFC). In addition, we compare this method to another approach that multiplies future maximum snow depth and the ratio of approximate function of the observed and simulated maximum snow depths in the present climate. To calculate the corrected maximum snow depth in the future

climate, SD_{fc}, the following equation is used at each site and for each year:

$$SD_{fc} = SD_f \times SD_o/SD_p. \quad \cdots \quad (3.2)$$

SD_f is the maximum snow depth in the future climate for each point and for each year, wherein the non-exceedance probability value in the future climate data is determined for each point and for each year. SD_o is the quantile value, which is calculated at the non-exceedance probability value in the AMeDAS distribution. SD_p is obtained from the distribution of the simulated snow depth in the present climate. Hereafter, this method is called ratio correction for future snow depths (FTRT).

Bias and RMSE are calculated in each region to evaluate the performance of the bias correction method. The corrected values are averaged over all years at each observation site. Bias and RMSE are weighted according to the number of the observation years at each observation site.

Furthermore, we classify each region using three classification methods to examine its impact on the performance of the bias correction. Two classification methods based on L-moments (Hosking and Wallis 1997) are tested. Observation sites in each region (referred to in Fig. 3.2) are classified into two sub-regions based on the size of the L-mean (GLME), and based on the coefficient of the L-variation (GLCV) of the annual maximum snow depth at every observation site. Regions in GLME and GLCV are divided into two sub-regions with the same number of observation points. The third classification method is based on the altitudes of the observation sites (GALT), to account for the topographic effect on climate in Japan. GALT is based on whether the altitudes are higher or lower than 100 m. However, RKN and RNG regions in GALT are not divided into sub-regions because most of the observation sites in these regions are located at high altitudes. The result without using the classification into sub-region (GNTC) is compared with those of the three classification methods.

Lastly, the heterogeneity measure H (Hosking and Wallis 1997) is used to determine whether the climatic features of the maximum snow depth at the observation sites in each sub-region are homogeneous. H is determined by calculating the second order of L-moments (L-cv), and its standard deviation (Vobs). Next, a virtual homogeneous region is created by determining the quantile values from random non-exceedance probabilities based on the Kappa distribution, same as the original data. This process is repeated to create many virtual regions, and the weighted standard deviation of L-cv for each virtual region (Vsim) is determined. Using the mean and standard deviation of Vsim, i.e. Vbar and Vsd, respectively, the heterogeneity measure H is defined by the following equation:

$$H = (Vobs - Vbar) / Vsd \quad \cdots \quad (3.3)$$

If the value of H is less than 1, the climatic features at observation sites in the region are considered similar. If the value of H is more than 2, they are considered dissimilar. On the other hand, values of H between 1 and 2 indicate possibly heterogeneous areas. We refer to the H in L-cv, where the values in each region are shown in Fig. 3.3. For GNTC and GALT, the values of H often exceed 2. In GLME,

the values of H exceed 2 in the two regions. In contrast, the values of H are less than 2 in all cases for GLCV. The implication is that the differences of the maximum snow depths among observation sites within regions are small in cases where the regions are classified based on L-cv.

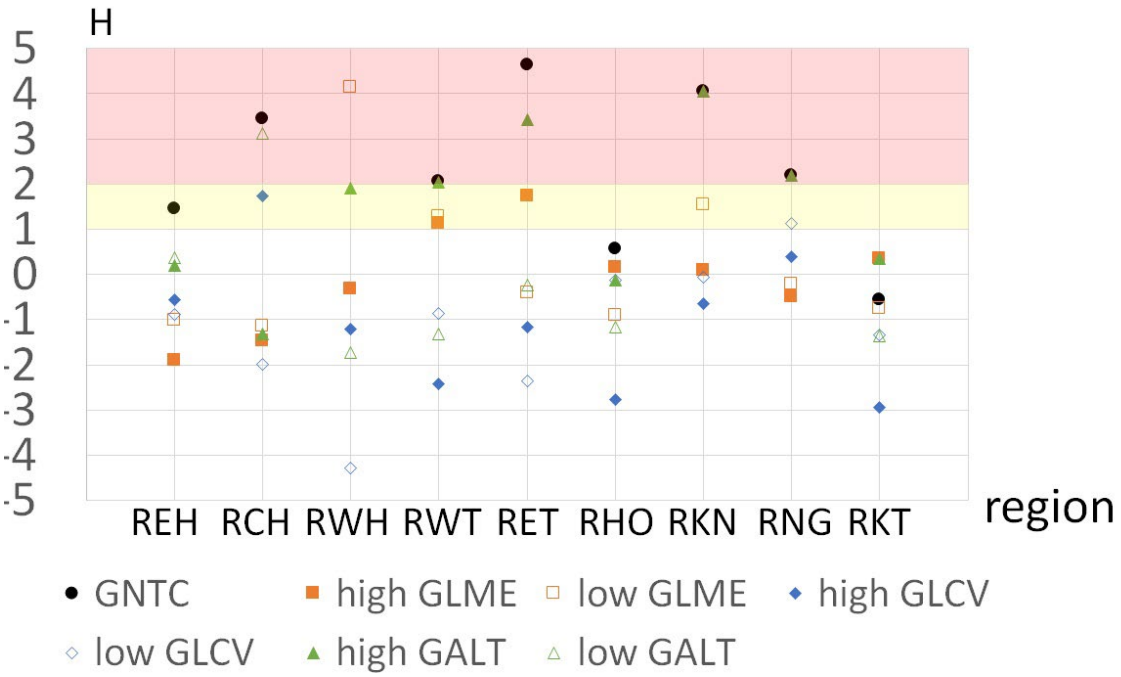

Figure 3.3. Heterogeneities of L-cv in each region for each classification method. Red and yellow shaded areas indicate definitely heterogeneous and possibly heterogeneous areas, respectively.

3.4 Results

Figure 3.4 shows the biases of maximum snow depths for each bias correction method in the present climate. Every bias correction method reduces the biases in all regions. The bias corrections decrease the bias averaged over all of Japan (hereafter referred to as ALL) by about 20 cm. These results indicate that bias correction is necessary for reproducing the present climate more accurately. Every classification into sub-regions (GLME, GLCV, and GALT) make the bias relatively small compared to the GNTC, except in the RET and RKT regions. In the RET region, the bias is higher for GLME than for GNTC. In the RKT region, the bias is slightly higher for GLCV than for GNTC. In other regions, the bias is generally small for GLCV compared with other classification methods. The GLME method also reduces the bias, but not as much as the GLCV. Note that the H for the GLCV is less than two in all regions (see Fig. 3.3). Hence, for conducting bias corrections more accurately, it is important to classify regions based on L-cv. In comparison with the CDFM method in Sasaki et al. (2013), the biases in CDFM and GLCV are 1.0 cm and 3.1 cm, respectively. The RMSE in GLCV (28.1 cm) is similar to that in the CDFM (27.1 cm). Accuracy of the new method is comparable to Sasaki et al. (2013).

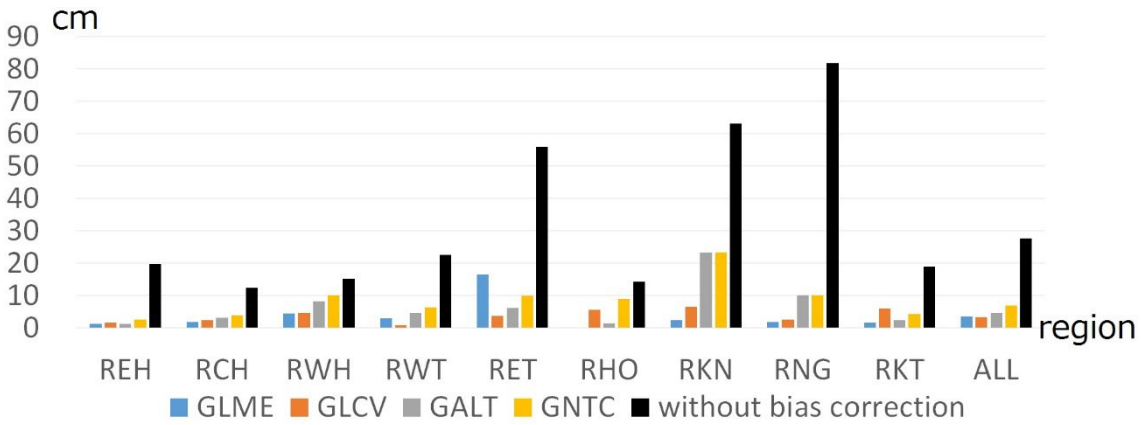

Figure 3.4. Bias of maximum snow depths in each region for each bias correction method and without bias correction method in the present climate.

We verify that this bias correction method can reduce biases in the future climate, by using the test sample estimate. Test sample estimate is described in Hill and Lewicki (2006). The data in the present climate is used for the verification, and divided into the former ten years (1980-1989) and the latter ten years (1990-1999). The former ten-year data are regarded as learning sample and the latter ten-year data are regarded as test sample. GLCV method is applied to these data. Figure 3.5 shows the biases of the test sample data. The bias correction improves reproducibility of the maximum snow depths. Bias of the maximum snow depths without bias correction averaged over ALL sites is 40 cm. By using FTFC and FTRT, the biases become 20 cm and 23 cm and RMSEs decrease from 63 cm to 28 cm and 41 cm, respectively. In the case that non-exceedance probability value is near 100, FTRT sometimes makes unnatural change. On the other side, FTFC always makes natural change. Therefore, GLCV is useful for maximum snow depths in the future climate, and FTFC is better than FTRT.

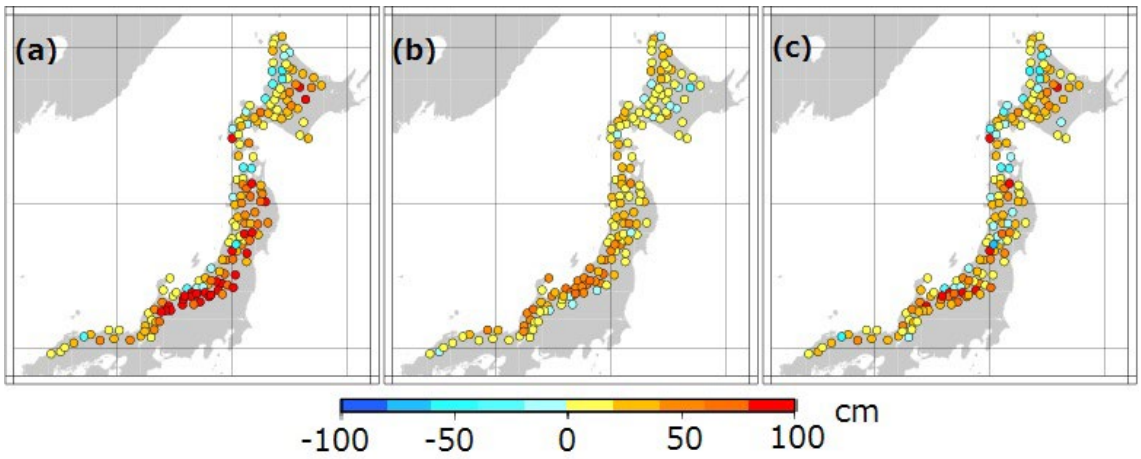

Figure 3.5. Bias of maximum snow depths of test data. (a) without bias correction (b) with FTFC correction (c) with FTRT correction.

Figure 3.6 shows the maximum snow depths and the changes in the maximum snow depth projected by using the GLCV bias correction method in the present and future climates. In the future climate, the maximum snow depths with GLCV averaged over ALL sites is 31 cm. Given that the average of the maximum snow depth in the present climate is about 85 cm, the value is projected to decrease by about 50 cm in the future climate. There are 20 white circles indicating maximum snow depths of 0 cm. Near the Pacific Ocean area, white circles increase. Those sites have small snow depths in the present climate. Figure 3.7 shows the maximum snow depths in the future climate averaged over each region. The maximum snow depths significantly decrease. In the present climate, maximum snow depths in RNG region and in RCH region are similar. However, the difference in maximum snow depths becomes large in the future climate, because projected maximum snow depth decreases by 80 cm in RNG region, but decreases by 40 cm in RCH region. In the present climate, the maximum snow depth in RKT region is 40 cm less than that in RNG region. In the future climate, difference in maximum snow depths between RNG region and RKT region becomes 1 cm. In the mountainous area, especially in RNG and in RHO, the quantity of the snow depth change is large, and the change is smaller than other areas in the northern part.

This result is consistent with Kawase et al. (2020b), which showed that in RNG and RHO, the snow fraction of precipitation decreases significantly under the future climate, resulting in a decrease in snow depth. In Hokkaido, on the other hand, they showed that the snow fraction of precipitation decrease is small, resulting in a smaller decrease in snow depth than in other regions.

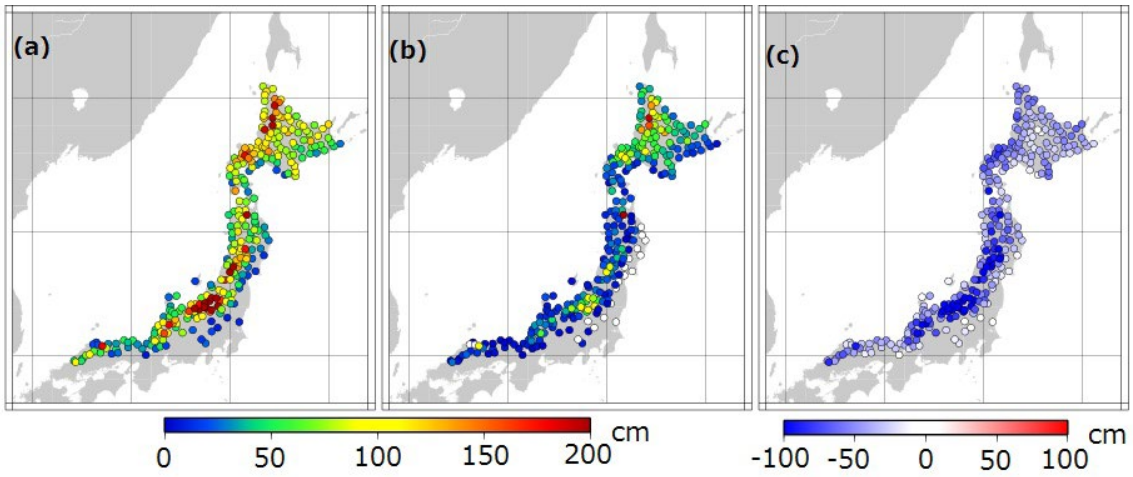

Figure 3.6. Average of the maximum snow depths (a) in the present climate (1980-1999) and (b) in the future climate (2080-2099). White circles indicate 0 cm of snow in the future climate. (c) Changes in the maximum snow depths.

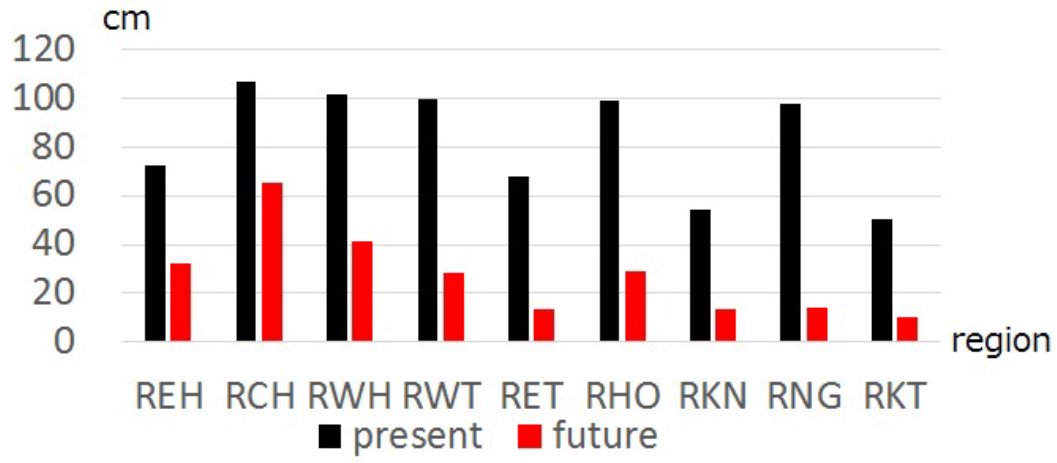

Figure 3.7. Average of the maximum snow depths in each region in the present and future climate.

3.5 Conclusion

We examined different methods of correcting the bias in simulations of annual maximum snow depth for more accurate projection of snow depths in the future climate. Our method involved classifying Japan into nine regions; each region was classified furthermore into two sub-regions based on three standards, namely, L-mean (GLME), L-cv (GLCV), and the altitudes of observation sites (GALT). With the GLCV method, the maximum snow depths in every sub-region were relatively homogeneous, and the bias was smaller compared to the other methods. We concluded that the GLCV method was the best among the three classification methods. The classification method proposed by Sasaki et al. (2013) requires a trial-and-error step, which makes automation of the process difficult. However, the GLCV method is easy to implement automatically on computer systems and produces very satisfactory results.

We confirmed that this bias correction method was useful for snow depth in the future climate by using the test sample estimate and carried out bias-corrected projections of future snow depths at the end of the 21st century. The maximum snow depths averaged over snowy districts in Japan were projected to decrease by about 50 cm and to become about 30 cm in the future. In the northern Japan area, the change in the maximum snow depth was smaller than those in the other areas. The snow depth was projected to decrease the most in the RNG (Nagano and Gifu) region, where maximum snow depths decreased by 80 cm.

In this chapter, we discussed the future prediction of snow depths, which was difficult to achieve with the 20 km model in Chapter 2, because the 5 km model had a large bias in reproducing snow depths, and it was difficult to discuss the future prediction using the data directly. However, the bias correction used in this chapter can only be applied to points where observation data is available, and in order to predict snow cover outside of observation points and reproduce snow cover distribution in more detail, it is necessary to use a model with finer resolution and better reproducibility.

Chapter 4. Future changes in early spring wind speed and surface warming acceleration in snow-covered areas

4.1 Introduction

Global warming drives an increase in surface air temperature that can lead to more frequent heavy precipitation events, a decrease in snow and ice cover, and changes in surface winds due to synoptic-scale variations in atmospheric circulation (Collins et al., 2013). Previous studies have reported increased heavy precipitation events over some regions (e.g., Emori and Brown, 2005; Shi and Durran, 2016). Increases in extreme snowfall events are projected for high mountainous areas, such as the Alps, the Rocky Mountains, and the high mountains in Japan (e.g., de Vries et al., 2014; Lute et al., 2015; Kawase et al., 2016), although Wang et al. (2018) demonstrated that the snow-covered area decreases under scenarios of 1.5 and 2.0 ℃ warming. Previous studies have also predicted future changes in surface winds. For example, Mclnnes et al. (2011) described results from the Coupled Model Intercomparison Project (CMIP) Phase 3 (CMIP3) models, which predicted enhanced surface wind speeds in some regions. Cheng et al. (2013) showed that the frequency of strong wind events in Canada would increase in future because of synoptic-scale circulation changes due to global warming. Hu et al. (2000) found that the East Asian winter monsoon would weaken because of changes to the land–ocean thermal contrast under global warming, and Kimoto (2005) and Hori and Ueda (2006) also predicted weakening of the East Asian winter monsoon under future climate conditions. However, these studies used global models that could not fully capture local topographic variability, which affects local wind patterns significantly; therefore, their ability to assess changes to near-surface winds was limited. Diffenbaugh et al. (2005) demonstrated that global-scale changes do not capture all global-warming induced climate change because fine-scale processes affect regional- to local-scale climate change.

Takemi (2013) showed that complex terrain could affect surface winds and stated that a more realistic representation of terrain was required to reproduce near-surface wind patterns. Mott et al. (2018) showed that complex topography in mountainous areas affects snow-cover patterns, and that local wind systems are affected by snow-cover heterogeneity. Terrain can be represented in regional climate models more realistically than in global climate models because the horizontal resolution of the former is generally higher. Beniston et al. (2007) used a regional climate model to demonstrate that the frequency of strong wind events in Europe will increase in the future. Hueging et al. (2013) predicted that potential wind-power generation would increase in Europe in response to changes in both synoptic-scale circulation and local wind systems. Kawase et al. (2015) showed that winter precipitation around the coast of the Japan Sea could decrease as the East Asian winter monsoon weakens under global warming.

Surface winds are affected by synoptic-scale circulation and by surface conditions. Future changes

to the distributions of vegetation, sea ice, and snow cover due to global warming will change surface roughness, and therefore affect wind speeds. Overland and Wang (2010) demonstrated that wind speeds were higher during seasons with less sea ice than in those with extensive sea-ice cover. Changes in snow cover may also influence the atmospheric boundary layer by altering ground heating rates. Little research has been conducted into how future changes will influence the wind in the surface boundary layer over snow-covered areas, particularly in areas of complex terrain such as the high mountains of Japan. Few studies (e.g., Hanafusa et al., 2013) have investigated local wind changes in East Asia that are attributable to global warming, despite the fact that the East Asian winter monsoon will weaken as a result of climate change (Hu et al., 2000). Convection-permitting regional climate model simulations are required to predict changes for snow cover and local climate over complex topography. For example, a regional climate model with a horizontal grid spacing of less than 2 km is required to calculate snow cover over the Rocky Mountains (Ikeda et al., 2010; Rasmussen et al., 2011) and Kawase et al. (2020a) highlighted that high resolution is important for simulations to reproduce present snow-cover conditions for the complex Japanese mountains, and to project future changes.

Here we investigate future changes to near-surface wind speed over snow-covered areas during the snow accumulation and snowmelt seasons, using results from long-term, high-resolution simulations calculated under current and future climate conditions. We also discuss the effect of snow cover on near-surface wind speed and temperature under future climate conditions.

4.2 Methods

4.2.1 Model and experimental design

Regional climate simulations are calculated using the Non-Hydrostatic Regional Climate Model (NHRCM; Sasaki et al., 2008) with one-way nesting. The NHRCM has horizontal resolutions of 2 and 5 km for the inner and outer domains, respectively (hereafter, NHRCM02 and NHRCM05, respectively; Figure 4.1). The model uses terrain-following coordinates for its 60 vertical levels, which are spaced at 25 hPa intervals between 1000 and 850 hPa, at 50 hPa intervals between 850 and 700 hPa, and at 100 hPa intervals between 700 and 100 hPa. Boundary conditions are derived from global climate simulations from the Meteorological Research Institute Atmospheric General Circulation Model version 3.2 (MRI-AGCM3.2) with 20 km horizontal resolution (Mizuta et al., 2012). The improved Meteorological Research Institute/Japan Meteorological Agency simple biosphere model (iSiB; Hirai and Oh'izumi, 2004; Ito et al., 2018) is used as the land surface model to simulate land processes, including snow accumulation and melt. Data are averaged from September to the following August for each year. Current and future climates are defined as the climates for 1980–1999 and 2076–2095, respectively. We use Representative Concentration Pathway 8.5 (RCP8.5) as the scenario for our projections of future climate. High-resolution simulations require intensive computational

resources, and an ensemble of many simulations is necessary to quantify the uncertainty for future model projections. We therefore consider model uncertainty by using a four-member ensemble of simulations from MRI-AGCM3.2 as boundary conditions for four NHRCM simulations. The ensemble was constructed by forcing the simulated changes in sea surface temperature (SST) to follow different spatial patterns. Cluster analysis of the SST changes projected by the 28 CMIP Phase 5 models (CMIP5) identified three spatial patterns (C1, C2, and C3), based on tropical SST spatial patterns, and these were used to force three of our MRI-AGCM3.2 ensemble members. The full CMIP5 ensemble of simulated SST changes were averaged over all CMIP5 models, and this pattern of SST change was used to force an additional ensemble member (C0). Details of the method for ensemble construction are provided in Mizuta et al. (2014) and Murata et al. (2017). Current and future climatological values are defined as 20 year means. Future climate data are taken as the average of the four future climate projections, which are forced by the four SST patterns (C0, C1, C2, and C3).

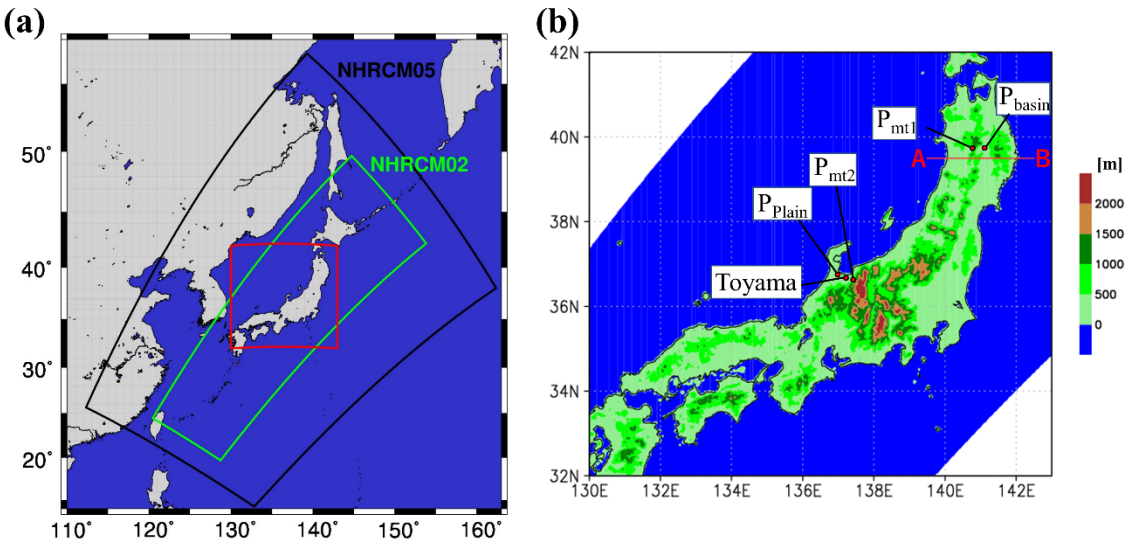

Figure 4.1. Model domains and topography. (a) Calculation domains, and (b) analysis region and topography in NHRCM02, enlarged from the red frame in (a).

Data from the Automated Meteorological Data Acquisition System (AMeDAS), managed by the JMA, are used to assess how accurately the simulations reproduce current climate conditions. Wind speed observations are available from around 700 stations in Japan, and we use the daily average wind speeds from these stations for the validation.

4.2.2 Performance of the NHRCM02

The NHRCM02 accurately reproduces the daily average 10 m wind speed (hereafter, WS). The annual mean value of observation, averaged over all AMeDAS stations, bias (model minus

observation), and the root mean square error (RMSE) are 2.8 m/s, 0.32 m/s, and 0.84 m/s, respectively. The spatial correlation coefficient is calculated by comparing the spatial distribution of wind speeds from the model with the observed distribution, resulting in a positive correlation (correlation coefficient r = 0.67). The values of bias, RMSE, and spatial correlation are 0.93 m/s, 1.2 m/s, and 0.54, respectively, for NHRCM05, so the reproducibility was improved by the higher resolution.

The NHRCM02 underestimates the annual mean WS in Japan and there are no regional patterns in the bias (Figure 4.2). The NHRCM02 also captures the current snow depth well. The snow depth mean value, bias and RMSE for March are 77 cm, 21 cm and 45 cm, respectively, and there is a strong spatial correlation between the model and observations (r = 0.82). The bias, RMSE, and spatial correlation values are 34 cm, 50 cm, and 0.74, respectively, for NHRCM05, so the higher resolution improved the reproducibility, but NHRCM02 also overpredicted the snow depth in mountainous areas (Figure 4.3).

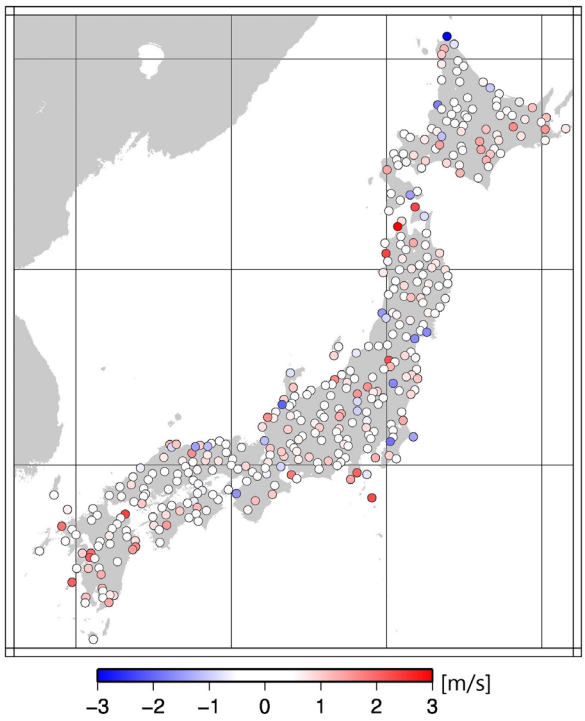

Figure 4.2. Bias in the annual mean model WS at the observation locations (m/s).

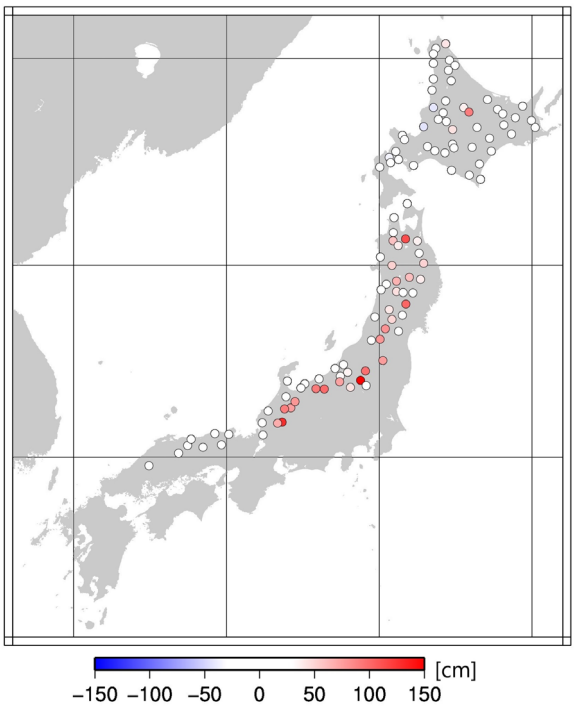

Figure 4.3. Monthly-mean daily-maximum snow depth bias for March at the observation locations (cm).

4.3 Future changes in wind speed

4.3.1 Future changes in wind speed over snow-covered areas

The NHRCM02 predicts a decline in WS over Japan during winter under future climate conditions (Figure 4.4a), which is consistent with the weakening of the winter monsoon projected by other studies because of global warming (e.g., Kimoto, 2005; Hori and Ueda, 2006; Kawase et al., 2015). The WS is projected to be lower in every month in many areas and in the winter average, but is projected to increase locally over the central Japan, especially around Toyama (Fig. 4.1b), and northeastern Japan, particularly in February and March (Figure 4.4b–4e).

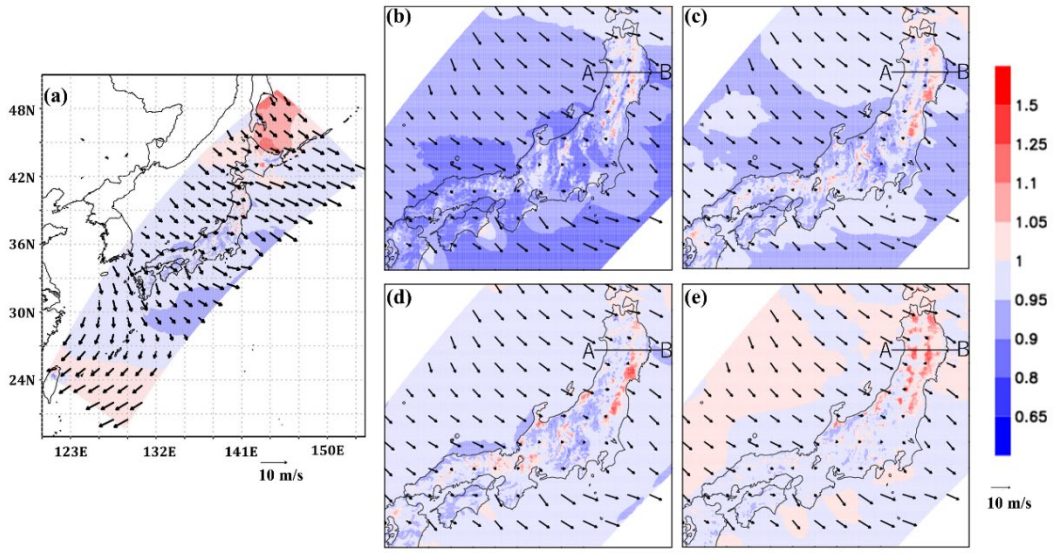

Figure 4.4. Near-surface wind speed under current climate conditions (arrows) and projected changes to WS under climate change (shaded; units are the ratio of future WS to current WS) for (a) December–March, (b) December, (c) January, (d) February, and (e) March. The future WSs are averaged of the C0, C1, C2, and C3.

We investigate the relationship between the changes in the number of snow-covered days and WS projected for March, since the present-day WS is higher over snow-covered areas than over snow-free areas in March (Figure 4.5). A snow-covered day is defined as a day when the maximum snow depth exceeds 10 cm. In the future projections, near-surface winds strengthen over areas where the number of snow-covered days decreases (black circles in Figure 4.6a). The wind becomes stronger at 92% of low-elevation model grid points where the number of snow-covered days decreases by 20 days (black bars in Figure 4.6c). However, the wind becomes stronger at only 4% of low-elevation grid points where the number of snow-covered days decreases by less than one day (black bars in Figure 4.6b).

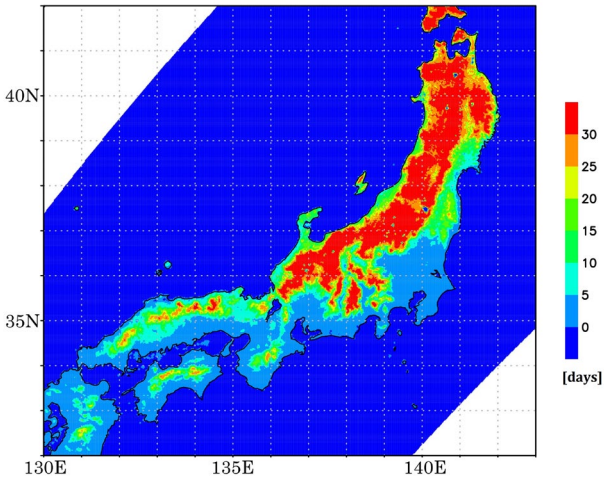

Figure 4.5. Number of snow-covered days in March under current climate conditions.

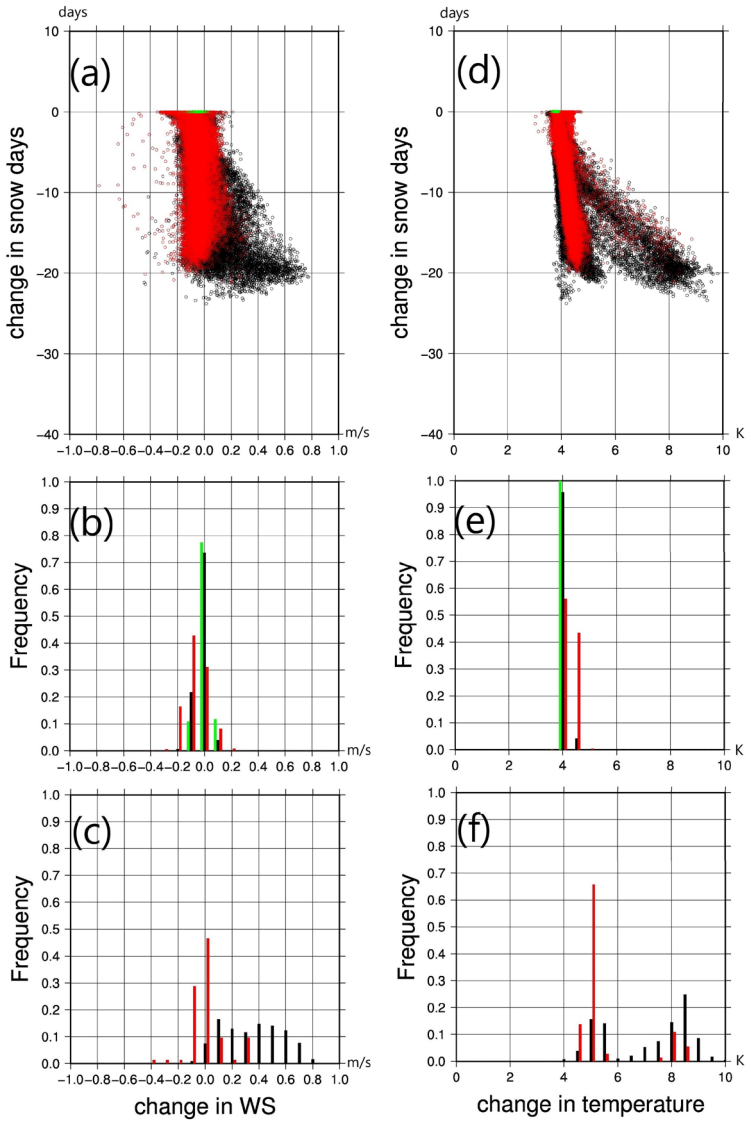

Figure 4.6. Relationship between the change in the number of snow-covered days, WS, and temperature. (a) Scatterplot of the future change in WS versus the change in number of snow-covered days, averaged over March at each grid point. Frequency distribution for the change in WS at grid points where the decrease in snow-covered days is (b) <1 day, and (c) 20 days. (d) Scatterplots of the future change in the 1.5 m air temperature versus the change in number of snow-covered days, averaged over March at each grid point. Frequency distribution for the temperature increase at grid points where the decrease in snow-covered days is (e) <1 day, and (f) 20 days. Black circles indicate low-elevation grid points (≤500 m altitude), red circles indicate high-elevation grid points (>500 m altitude), and green circles indicate grid points with no snow cover under either current or future climate conditions. The values under the future climate conditions are averaged of C0, C1, C2, and C3.

The relationship between the changes projected for WS and for the number of snow-covered days is clearer at low elevations than at high elevations. The 1.5 m air temperature increases because of reduced snow cover, particularly at low elevations (Figure 6d). The 1.5 m air temperature rises by 4.2 and 3.8 ℃ in areas with and without snow cover, respectively, relative to current climate conditions. Reduced snow cover caused by global warming can promote local increases in surface air temperature due to the reduction in surface albedo (e.g., Matsumura and Sato, 2011; Scherrer et al., 2012). The increase in surface air temperature therefore follows a reduction in the number of snow-covered days (Figure 4.6d).

Surface conditions respond differently to reduced snow cover at low and high elevations, as shown in Figure 4.6. The increase in surface air temperature is projected to exceed 5 ℃ at 80% of low-elevation grid points where the number of snow-covered days decreases by 20 (black bars in Figure 6f), but the increase is less than 5 ℃ at 82% of high-elevation grid points that experience this same reduction in snow cover (red bars in Figure 4.6f). No increase exceeding 5 ℃ occurs at any grid points where the decrease in snow-covered days is less than one day (all bars in Figure 4.6e). A clear relationship exists between temperature increase and changes in the number of snow-covered days at low elevations. The temperature increases are much smaller at high elevations than at low elevations, and the increases are slightly larger in areas that record a reduction in snow cover than in those areas with no current snow cover.

4.3.2 Impact of changes in synoptic-scale atmospheric circulation on wind speed over snow-covered areas

In addition to being affected by changes in local snow cover, near-surface winds may change in response to SST changes in the Sea of Japan, and/or to changes in synoptic-scale atmospheric circulation. Previous studies have highlighted the impact of SST on regional climate in the Sea of Japan (e.g., Sato and Sugimoto, 2013; Takahashi and Idenaga, 2013; Yasunaga and Tomochika, 2017). The boundary conditions for our regional climate simulations are from four global climate simulations that are forced by different patterns of SST change (i.e., C0, C1, C2, and C3). The SST increases in C1 and C3 are the smallest and largest among the four experiments, respectively. The March temperature increase in C1 is around 1 ℃ smaller than that in C3 (Figure 4.7). Changes to the synoptic-scale circulation differ in these two experiments because of the different SST boundary conditions (Figure 4.8). In the simulation using C3-forced boundary conditions, sea level pressure increases in eastern Japan and decreases in western Japan, and the East Asian winter monsoon weakens; these changes are not observed during the experiment that employs boundary conditions forced by C1, and are therefore attributable to the large SST increase in C3 relative to C1. In contrast, the increase in wind speed at each grid point follows the decrease in snow-covered days similarly in the experiments forced by C1 and C3, regardless of the different increases in SST in these two

experiments. Where there is no snow cover, wind speed becomes stronger in the C1-forced experiment than in the C3-forced experiment; however, the wind strengthens equally in both experiments when the number of snow-covered days decreases. This shows that local changes, such as those caused by changing surface conditions, are driven by the same mechanisms everywhere, irrespective of boundary conditions such as SST.

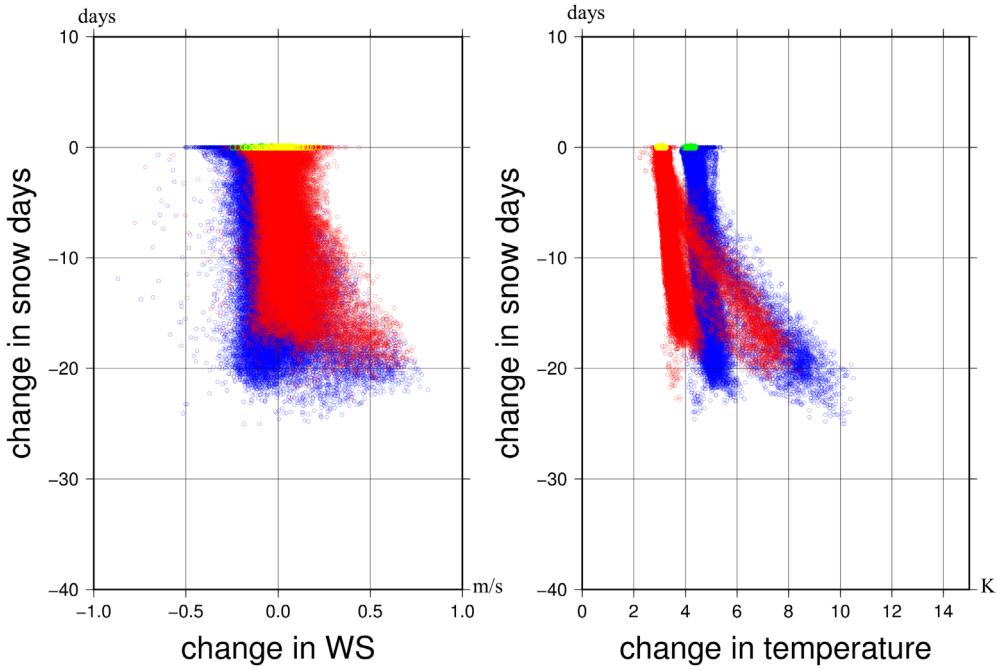

Figure 4.7. Impact of SST variation on the number of snow-covered days, WS, and temperature. Scatterplots of (a) projected WS changes versus the change in number of snow-covered days, and (b) projected temperature changes versus number of snow-covered days. Red circles are the C1 results, yellow circles are C1 grid points with no snow cover under current climate conditions, blue circles are the C3 results, and green circles are C3 grid points with no snow cover under current climate conditions.

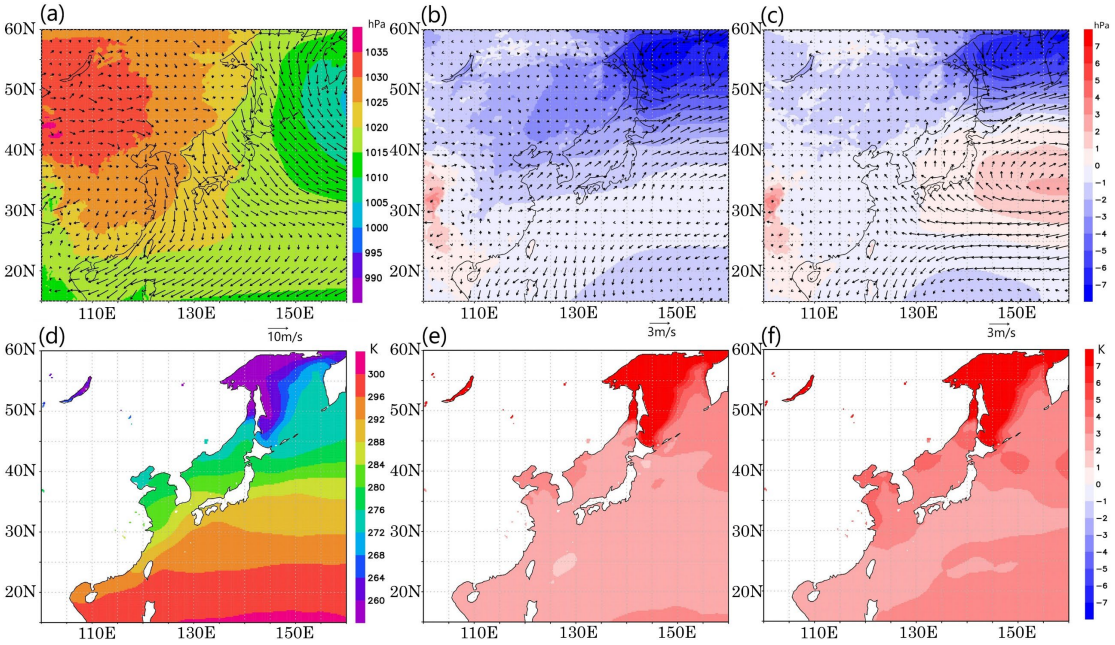

Figure 4.8. Impact of SST variation on circulation changes in MRI-AGCM3.2 simulations. (a) Simulated sea level pressure (shaded) and wind (vectors) in March under current climate conditions, and simulated changes in sea level pressure (shaded) and wind (vectors) in March (b) under C1 forcings, and (c) under C3 forcings. (d) Simulated March SST under current climate conditions, and simulated SST changes in March (e) under C1 forcings, and (f) under C3 forcings.

4.4 Mechanisms for projected future wind strengthening

Rapid ground heating as a result of reduced snow cover increases instabilities near the surface, which can strengthen near-surface winds because stability is correlated with wind speed (Garratt, 1992). In addition, as the snow cover disappears and the ground is exposed, the roughness length increases, and the increase in roughness length also increases instability. Stability (dPT) is defined as:

$$dPTXX = PT(XX - 50\ hPa) - PT(XX\ hPa), \quad \cdots \quad (4.1)$$

where dPT is the difference in potential temperature (PT) between a specific pressure layer (XX) and a layer 50 hPa above XX. A higher value for dPT indicates a more stable layer.

Figure 4.9 shows a vertical cross-section of PT and dPT in March along the line marked AB in Figures 4.1b and 4.4b–e. The increase in PT due to global warming exceeds four Kelvin and increases with elevation (contours in Figure 4.9b). The increase in PT at low elevations and in basins is greater than the increase at the same pressure level over the ocean. The increase in PT at high elevations is similar to the increase in ambient PT at the same pressure level over the ocean. Figure 4.9c shows the stability anomaly (the deviation of the stability from the mean value) at each pressure level under current climate conditions. Remarkably stable layers are found at low elevations and in basins. The stability is relatively constant across pressure levels at high elevations. The change in dPT projected

by the simulations is plotted in Figure 4.9d, which shows that most atmospheric layers become more stable under future climate conditions, but atmospheric stability will decrease at low elevations and in basins where the atmosphere is currently more stable.

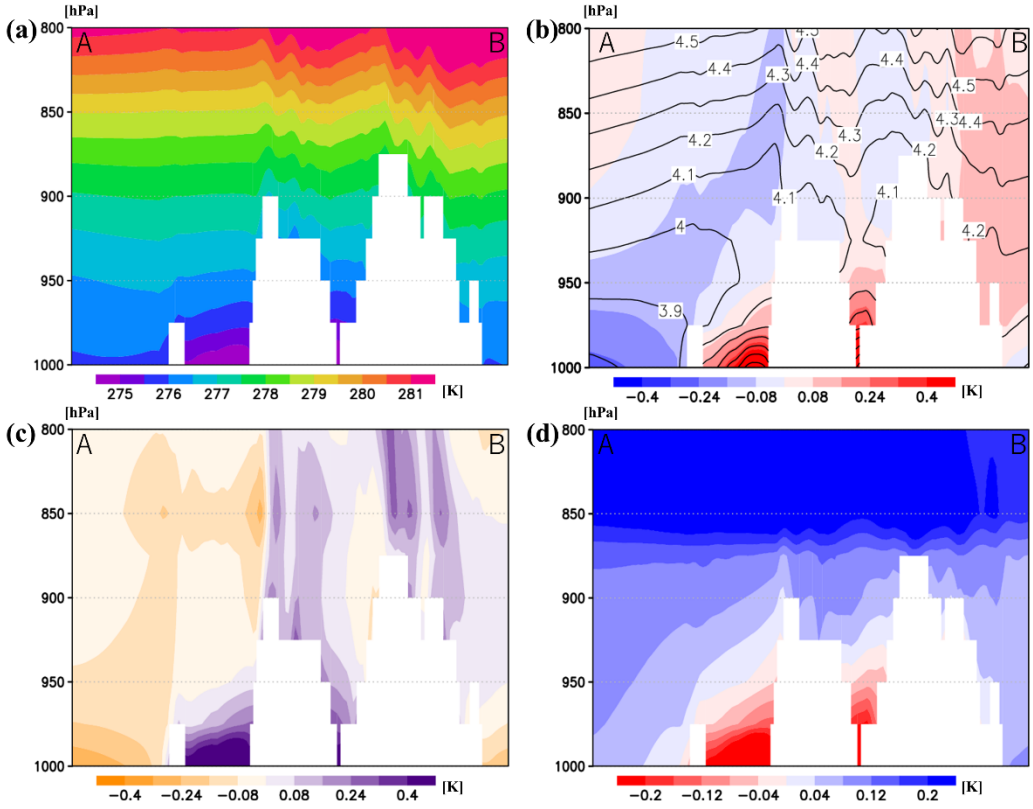

Figure 4.9. Cross-sectional view of the monthly mean PT and dPT for March along the line marked AB in Figure 4.1b. (a) PT under current climate conditions, (b) projected change in PT under future climate conditions (contours; units: K) and deviation of projected future PT from the pressure-level averaged future value (shading; units: K), (c) deviation of dPT from the pressure-level averaged dPT under current climate conditions, and (d) projected change in dPT under future climate conditions, relative to current climate conditions. Gray shaded areas indicate missing data, where the land surface pressure exceeds the plotted pressure level. The values under the future climate conditions are averaged of C0, C1, C2, and C3.

Figure 4.10a (4.10b) shows the changes projected for dPT1000 (dPT950) and WS under future climate conditions at all land grid points in Figure 4e. dPT1000 and dPT950 represent the near-surface at low elevations (close to 0 m above sea level; m a.s.l.) and at high elevations (around 500 m a.s.l.), respectively. Data are only included in Figure 4.10a (Figure 4.10b) from grid points where the 1000 hPa (950 hPa) height exceeds the model land surface height. dPT1000 is inversely proportional to WS, and changes projected for WS at low elevations are related to changes in the stability of the surface

boundary layer. Figure 4.10b shows no correlation between the changes projected for dPT950 and for WS, because the near-surface winds are not projected to strengthen and the projected stability changes are small. Atmospheric stability under current climate conditions is an important driver for enhanced surface warming and strengthening winds. Figure 4.10c (4.10d) shows the relationship between dPT1000 (dPT950) and the projected changes in dPT1000 (dPT950) at low (high) elevations. The magnitude of projected change in stability under future climate conditions is constant and is independent of the dPT value under current climate conditions for areas with no snow cover. A strong deterioration in stability is projected at low elevations where dPT1000 is high under current climate conditions (Figure 4.10c), and some smaller changes are projected for stability at high elevations, regardless of dPT950 under current climate conditions (Figure 4.10d).

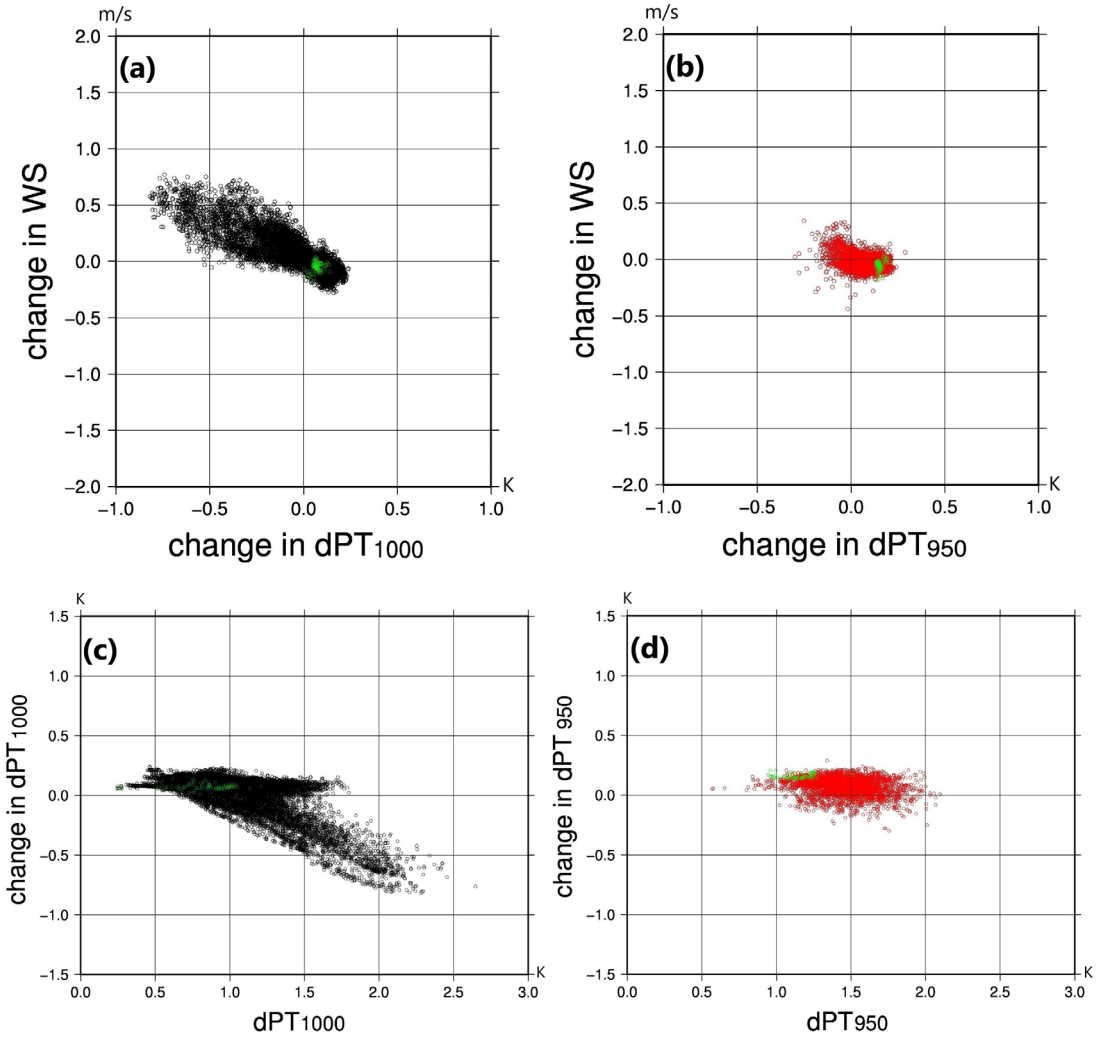

Figure 4.10. Scatterplots of changes projected for dPT and WS under future climate conditions for (a) dPT1000 and (b) dPT950. Scatterplots of changes projected for dPT and dPT values under current climate conditions for (c) dPT1000, and (d) dPT950. Black circles indicate low-elevation grid points (≤500 m altitude), red circles indicate high-elevation grid points (>500 m altitude), and green circles indicate locations with no snow cover under both current and future climate conditions. Only low-elevation grid points are plotted in (a) and (c), and only high-elevation grid points are plotted in (b) and (d) to investigate the near-surface changes in dPT and WS. The values under the future climate conditions are averaged of C0, C1, C2, and C3.

4.5 Hypothesis verification and discussion

4.5.1 Future changes in daytime and nighttime wind speed

Our results suggest that the presence, or absence, of a stable atmospheric layer under current climate conditions influences future changes in wind speed over snow-covered areas. If the presence,

or absence, of a stable layer created by the presence of snow affects the predicted future drastic changes in wind and temperature, differences will be observed between the changes projected for daytime and nighttime wind speeds. Table 4.1 shows the changes in daytime (00:00–05:00 UTC) and nighttime (12:00–17:00 UTC) wind speeds projected for from December to March for a grid point in a basin, a grid pint in a plain and two grid points on mountain tops, labeled P_{basin} (167 m a.s.l.), P_{plain} (37 m a.s.l.) P_{mt1} (1044 m a.s.l.) and P_{mt2} (746 m a.s.l.), respectively in Figure 4.1b. At P_{basin}, wind speed is projected to increase significantly by 12% and 26% during the day in December and March, respectively. The wind at P_{plain} is also 13% and 27% stronger during the day in December and March, respectively. On the other hand, the changes in nighttime wind speed are smaller than those in daytime wind speed at P_{plain} and P_{basin}, except for P_{basin} in December. The nighttime wind significantly weakens at P_{basin} in December. At the two mountain grid points, the wind speeds decrease in December and the changes in wind speed are small in March.

During the day, surface heating via solar radiation is inhibited by the presence of snow cover at P_{basin} and P_{plain}, and a stable near-surface layer exists under current climate conditions. Under future climate conditions, the absence of this snow cover means that there is no stable layer, and the wind is therefore stronger. During the night, the stable layer exists with or without snow-cover because of no solar radiation. The effect of snow cover on the longwave emissivity is small (Hartmann 2016). Thus, there is no strengthening of the wind, and the wind tends to weaken in response to changes in the synoptic field (Fig. 4.4 b-c). In December, the wind speed becomes smaller at the mountainous grid points, which relates to the weakened synoptic-scale wind speed (Fig. 4.4b). The difference of future changes in wind speed during day and night are small at the two mountain grid points. The absence of a strong, stable near-surface atmospheric layer at higher elevations under current climate conditions means that changes in wind speed are smaller here than in basins and at lower elevations. The collapse of the current stable atmospheric layer that resulted in the strengthening of daytime wind speeds at P_{basin} and P_{plain} is not projected to occur at P_{mt1} and P_{mt2}. The changes projected for daytime wind speed at P_{mt1} and P_{mt2} are therefore small, despite the reduction in number of snow-covered days. These differences in projected changes for daytime and nighttime wind speeds verify our hypothesis.

Table 4.1. Changes projected for daytime and nighttime wind speed and for the number of snow-covered days at a basin location (P_{basin}), a plain location (P_{plain}), and at two mountain tops (P_{mt1} and P_{mt2}). The asterisk indicates statistical significance.

	P_{basin}		P_{plain}		P_{mt1}		P_{mt2}	
	Dec	Mar	Dec	Mar	Dec	Mar	Dec	Mar
Daytime wind speed	+12%*	+26%*	+13%*	+27%	-2%	+3%	-6%*	-1%
Nighttime wind speed	-10%*	+1%	+2%	+12%*	-3%	+1%	-7%*	-2%
The number of snow-covered days	-12	-19	-17	-15	-2	0	-14	-13

4.5.2 Verification using observation data

We use the AMeDAS observation data to confirm our hypothesis. If the hypothesis is correct, wind speeds should be statistically stronger at stations with no snow cover. In northeastern Japan, cold air outbreaks from the continent drive synoptic-scale northwest winds in winter (i.e., the winter monsoon), and near-surface winds are stronger on days with cold air outbreaks than on days without. To investigate the influence of snow cover on near-surface wind speed, we therefore first identify days with cold air outbreaks using wind observations from a high-altitude (890 m) station (Sukayu station, N040.65 E140.85), where the wind is controlled primarily by synoptic-scale atmospheric circulation. A cold air outbreak occurrence is defined as a day when the wind speed exceeds 5 m/s and the predominant wind direction is northwesterly. The near-surface wind speed is taken from values recorded in March between 1980 and 1999. March is in the snow-melting season for low elevations in this region.

Figure 4.11 shows the observed near-surface wind speed at 32 locations for days with and without cold air outbreaks, where the snow depth exceeded 10 cm, and where there was no snow cover. On days with cold air outbreaks, wind speeds were 4% stronger where no snow cover was present than those recorded where snow depth exceeded 10 cm (Figure 4.11a), and on days without cold air outbreaks, wind speeds were 6% stronger when there was no snow cover (Figure 4.11b). The difference in wind speed is only statistically significant for those days with no cold air outbreaks. On days with cold air outbreaks, the effect of snow cover is reduced because strong winds prevent the formation of a stable near-surface layer. These results support our hypothesis that the presence or absence of snow cover influences future changes in wind speed over snow-covered areas.

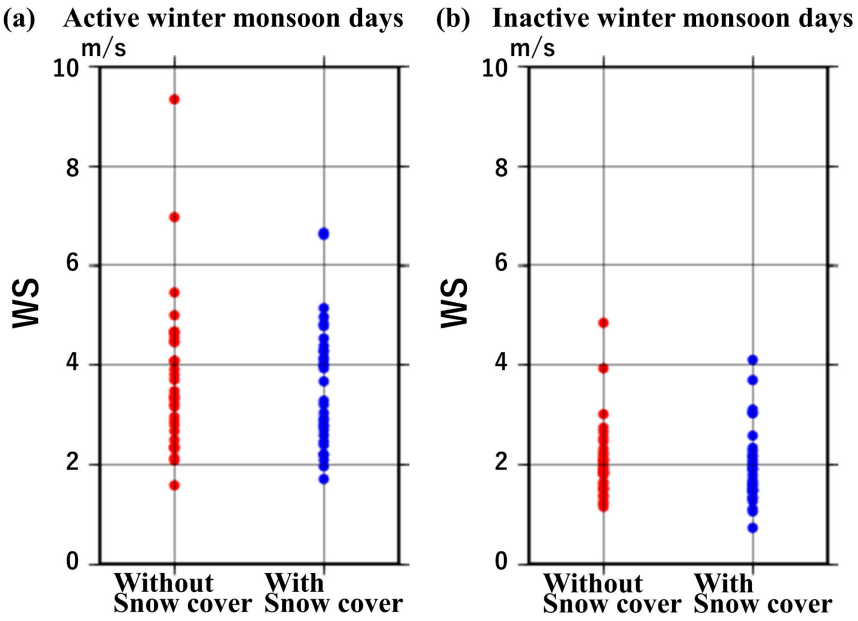

Figure 4.11. Observed wind speed in March at AMeDAS stations where the snow depth exceeds 10 cm, and where there is no snow cover on (a) active winter monsoon days, and (b) inactive winter monsoon days.

4.5.3 Impact of snow cover on local wind system

Consider the effect of this mechanism on local winds, e.g., föhn phenomenon. When local winds are blowing, wind speed enhancement due to the loss of snow cover cannot be expected to occur due to low stability. The Toyama Plain (around 36.7N 137.2E) is an area with snow cover in winter in the present climate. As with the basins in the northeastern Japan, the wind weakness over the Toyama Plain weakens in February and March under the future climate (Fig. 4.4d-e). Since the Toyama Plain is located at the north of the mountains, it is known that a föhn phenomenon occurs when a southerly wind blow (Arakawa et al. 1982; Ishizaki and Takayabu. 2009).

We examined whether the wind speed at the onset of the föhn phenomenon in the Toyama Plain is affected by the presence or absence of snow cover using the observational data in Toyama meteorological station (Fig. 4.1b). As a result, when the southerly wind speed was over 5 m/s, the wind speed difference from the Kamiichi AMeDAS located in the mountainous area was more than 15% stronger under the condition without snow cover than under the condition with snow cover (Table 4.2). Considering the cause of the strengthening of local wind speeds due to the decrease in snow cover, another mechanism can be considered as follows. In the föhn phenomenon, the wind blows along the mountain and accelerates as it moves down. In this case, when the roughness length is reduced due to the presence of snow cover, the wind leaves the mountain surface faster. When there is no snow cover, the roughness length becomes larger and the wind tends to blow along the mountain surface, leading

to long terrain-following descent and strengthening the wind. This mechanism is not limited to the Toyama Plain, but can also occur in other areas where local winds blow. Isolation of which mechanism is responsible for wind speed enhancement and verification of the mechanism of local wind enhancement are issues for future study.

Table 4.2. Change in wind speed in Toyama with and without snow cover during a föhn phenomenon. The asterisk indicates statistical significance.

	Dec	Mar
Wind speed difference between Toyama station and Kamiichi AMeDAS with snow cover (m/s)	4.3	5.0
Difference of wind speed (%)	+15*	+18*

4.5.4 Summarized processes of future changes in surface wind speed over snowy areas

The schematic diagrams in Figure 12 illustrate the processes that influence future changes in wind speed over snow-covered areas. Areas of snow cover will decrease in Japan as a result of global warming (Hosaka et al., 2005). Under current climate conditions, a stable layer develops over snow-covered areas at low elevations and in basins (Figure 4.12a). As the number of snow-covered days decreases in future, this near-surface stability will deteriorate. The collapse of the stable layer strengthens near-surface winds through vertical momentum exchange with the low-level jet that exists in the stable layer, which in turn accelerates the increase in surface temperature through increased thermal exchange (Figure 4.12b). In contrast, no increase in wind speed and surface temperature occurs at high elevations, even if global warming causes the snow cover to disappear entirely, because no strong stable layer forms under current climate conditions.

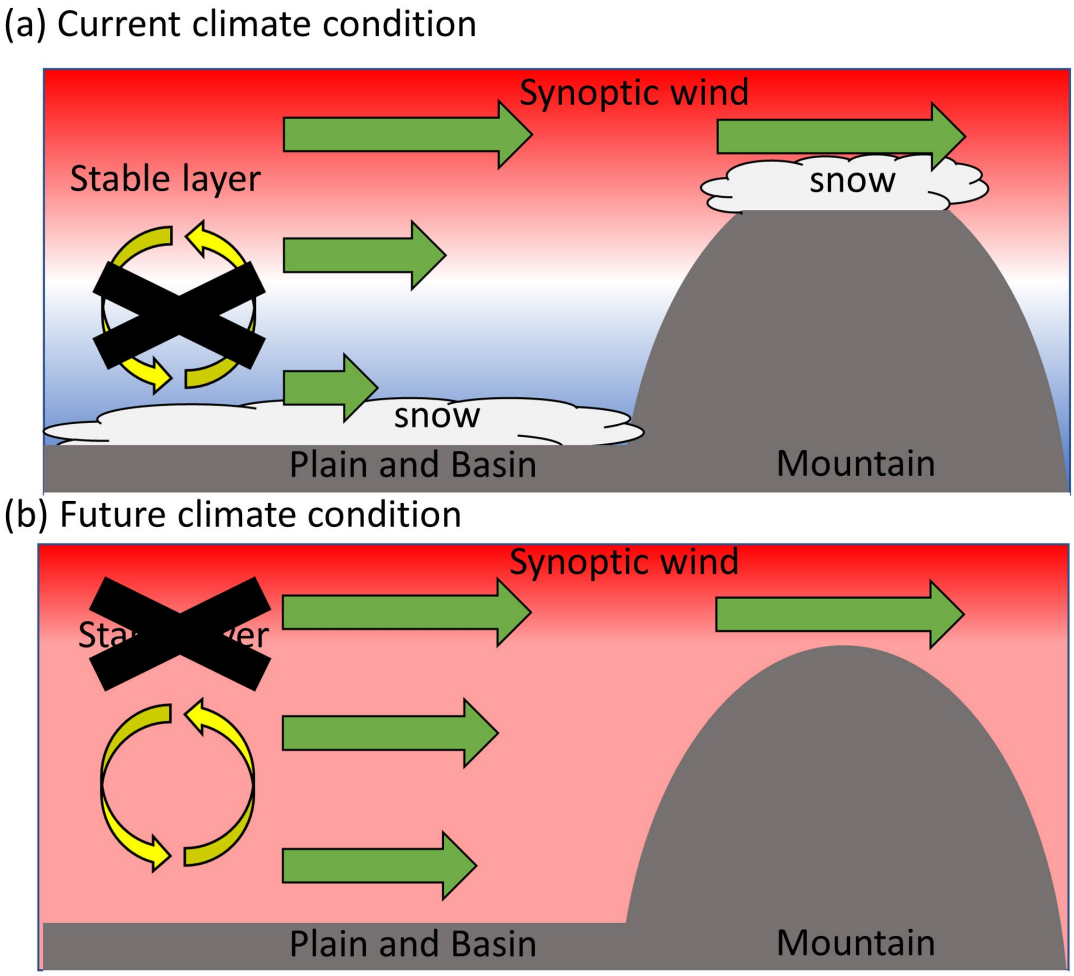

Figure 4.12. Schematic diagrams illustrating the processes that influence future changes in wind speed over snow-covered areas under (a) current climate conditions, and (b) future climate conditions. Background colors show the potential temperature, with red indicating warm and blue indicating cold.

4.6 Conclusions

Previous studies have shown that synoptic-scale near-surface winds will weaken around Japan in winter and early spring because of the weakening of the East Asian winter monsoon under future climate conditions. In this chapter, we analyzed convection-permitting regional climate simulations and found that near-surface winds would strengthen locally over some snow-covered areas in Japan. Under current climate conditions, a strong, stable atmospheric layer exists over snow surfaces. A reduction in snow cover as a result of global warming would accelerate local surface warming because of the reduced surface albedo. Surface warming prevents the formation of a stable atmospheric boundary layer, and thus strengthens near-surface winds and accelerates surface temperature increases through vertical momentum and thermal exchanges with the low-level jet. The observation data partly

support this theory. A momentum balance analysis would reinforce this mechanism.

The future collapse of the stable atmospheric near-surface layer can only occur at low elevations and in basins, because the stable layer does not exist at high elevations under current climate conditions. Therefore, the strengthening of the wind and acceleration of temperature increases that follow the collapse (or deterioration) of the layer will not occur at high elevations. The presence, or absence, of the stable layer explains the difference between future changes projected for snow-covered areas at high and low elevations. We found that the existence of a stable layer under current climate conditions explained local differences between future changes projected for near-surface wind speed and air temperature. Our methodology and results may be used to improve understanding for other snow-covered areas with complex topography. The strengthening of the wind and acceleration of surface warming that are projected under future climate conditions will affect the duration of winter and increase evaporation, which may affect ecosystems due to changes in the range of activities of living organisms.

Chapter 5 Conclusion

In this study, we investigated climate change in Japan using an NHRCM-generated dataset. We evaluated the reproducibility of the NHRCM at different resolutions and investigated climate change and local climate change in Japan. Concerning climate change, we considered snow cover and studied the differences in the number of days of snow cover across Japan depending on the level of warming, future changes in snow cover at AMeDAS sites, and effects of future snow cover reduction in the atmosphere.

The reproducibility of the NHRCM dataset was investigated using the d4PDF dataset with 20-km horizontal resolution and the SOUSEI/TOUGOU dataset with 5- and 2-km horizontal resolutions. NHRCM with 20-km horizontal resolution reproduced temperature and precipitation and improved the precipitation frequency compared with the global model with 60-km horizontal resolution. The results show that higher resolution improved the reproducibility of the precipitation distribution.

Next, comparing the climate change of Japan with that in the world, we found that the projected temperature increase in Japan is 1.4 times larger than that in the world and that this relationship can be maintained regardless of the level of warming. In terms of precipitation, annual precipitation is not linearly related to global warming, whereas strong precipitation is linearly related to a temperature increase of 6%–7% per 1 K. The change in the number of days of snow cover was projected to decrease rapidly because of an increase in temperature. However, the snow depth was not considered in the 20-km model because of a poor representation of elevation and topography.

In Chapter 3, the 5-km model was used to project future snow depths, and although it reproduced the topography better than the 20-km model, the bias was too large to adequately project the future climate using the model output values. A bias correction using observed values was considered, and the annual maximum snow depth, which is available once annually, was grouped using regional frequency analysis and was corrected using the cumulative density function to improve reproducibility. Future projections using this correction showed a large decrease in the snow depth in mountainous areas of the Chubu region, whereas the decrease was small in the central part of Hokkaido. This correction method improved the reproducibility of the snow depths at the observation points and allowed accurate future projections. However, the projections were made only at the points where observation data were available, and a higher resolution was required for future projections outside the observation points.

In Chapter 4, the 2-km model with the higher resolution reproduced snow depths even better than the 5-km model. Therefore, these data were used for future projections in locations with no observation data. In areas where snow cover will decrease in the future, an increase in the local temperature accelerated because of albedo change. Therefore, in regions where a stable layer is formed over the snowpack under the present climate, the stability of the surface boundary layer decreases and the

exchange of momentum with the atmosphere caused wind speed enhancement. This mechanism is particularly noticeable at low altitudes. At high altitudes, the stability layer was less likely to form because of the influence of the synoptic field under the present climate, meaning that the stability of the surface boundary layer decrease in the future climate fails to occur, thereby preventing wind speed enhancement.

This study using regional climate models has contributed to our understanding of climate change in Japan. However, the bias of regional climate models still exists, although it has been reduced using higher resolutions. Reducing bias and improving reproducibility are issues that require solving continuously. Particularly, reproducing snow depth is difficult because it is affected by the bias of other weather elements (e.g., surface temperature and precipitation). Additionally, the representation of the observed data is also a difficult factor to handle. One of our themes is improving the land surface process and is related to the reproducibility of ground elements. To improve the land surface processes, we introduce sophisticated snow models and upgrade the urban models.

Even with reduced bias, there is still uncertainty due to model characteristics. To mitigate this, we are developing other regional climate models in addition to NHRCM. The use of regional climate models based on the incumbent climate model asuca (Ishida et al. 2022) allows for multi-modeling of regional models and discussing uncertainty due to regional models in future projections. Additionally, SSTs selection should be considered because of the large influence of future patterns of SST change. One issue to be addressed is the study of future projections that consider the effect of different future trends in sea surface temperatures.

The annual maximum snow depth largely affects water resources, and the large decrease of the snow depth in the future climate in central Japan can affect future agriculture. Therefore, adaptation to the future climate using future projections should also be considered. Changes in urban areas and land use were not considered in this future projection. More detailed information on future changes in land use due to population change and changes in economic activity would allow us to discuss more localized effects of global warming. More detailed projections of warming in urban areas will be useful in projecting future changes in the number of heatstroke patients due to global warming.

The progress of global warming is decisive, and many problems, such as increased strong precipitation, drought, and decreased snow cover, are attributed to global warming. High-resolution, multi-ensemble data will be useful in developing adaptation strategies for these problems. Applying high-resolution large ensemble data can provide estimates of the maximum damage and probabilities of changes that are likely to occur. Furthermore, the development of multi-model ensembles that consider the effects of SSTs will provide datasets for generating more accurate information.

Reference

Arakawa, S., Yamada, L., and Toya, T., 1982: A study of foehn in the Hokuriku district using AMeDAS data. *Pap. Met. Geophys.*, 33, 149–163

Beniston, M., Stephenson, D. B., Christensen, O. B., Ferro, C. A. T., Frei, C., Goyette, S., Halsnaes, K., Holt, T., Jylhä, K., Koffi, B., Palutikof, J., Schöll, R., Semmler, T., & Woth, K., 2007: Future extreme events in European climate: An exploration of regional climate model projections. *Climatic Change*, 81, 71–95.

Cheng, C. S., Lopes, E., Fu, C. & Huang, Z., 2013: Possible impacts of climate change on wind gusts under downscaled future climate conditions: updated for Canada. *J. Clim.* 27 1255–70.

Collins, M., Knutti, R., Arblaster, J., Dufresne, J. L., Fichefet, T., Friedlingstein, P., Gao, X., Gutowski, W. J., Johns, T., Krinner, G., Shongwe, M., Tebaldi, C., Weaver A. J., & Wehner, M., 2013: Long-term Climate Change: Projections, Commitments and Irreversibility. In Stocker, T.F., D. Qin, G.-K. Plattner, M. Tignor, S.K. Allen, J. Boschung, A. Nauels, Y. Xia, V. Bex and P.M. Midgley (Eds.), *Climate Change 2013*, *The Physical Science Basis*. *Cambridge University Press*, 1029–1136.

de Vries, H., Lenderink, G., & vanMeijgaard, E., 2014: Future snowfall in western and central Europe projected with a high-resolution regional climate model ensemble. *Geophys Res. Lett.,* 41. 4294–4299. doi:10.1002/2014GL059724

Diffenbaugh, N. S., Pal, J. S., Trapp, R. J., & Giorgi, G., 2005: Fine-scale processes regulate the response of extreme events to global climate change. *Proc. Natl. Acad. Sci. USA, 102(15)*, 774–15 778.

Emori, S., & Brown., S. J., 2005: Dynamic and thermodynamic changes in mean and extreme precipitation under changed climate. *Geophys. Res. Lett.,* 32, L17706.

Fujita, M., Mizuta, R., Ishii, M., Endo, H., Sato, T., Okada, Y., Kawazoe, S., Sugimoto, S., Ishihara, K., and Watanabe, S., 2019: Precipitation changes in a climate with 2-K surface warming from large ensemble simulations Using 60-km global and 20-km regional atmospheric models. *Geophys. Res. Lett.*, 45, doi:10.1029/2018GL079885

Gao, X., Zhu, Q., Yang, Z., Liu, J., Wang, H., Shao, W., Huang, G., 2018: Temperature Dependence of Hourly, Daily, and Event-based Precipitation Extremes Over China. *Sci. Rep.* 8:17564. doi:10.1038/s41598-018-35405-4

Garratt, J. R., 1992: The Atmospheric Boundary Layer. *Cambridge Univ. Press, Cambridge, U.K.*

Giorgi, F., Bi, X., & Pal, J., 2004: Mean, interannual variability and trends in a regional climate change experiment over Europe. II: climate change scenarios (2071–2100). *Climate Dynamics*, 23, 839-858, doi:10.1007/s00382-004-0467-0.

Giorgi, F., Im, E.-S., Coppola, E., Diffenbaugh, N. S., Gao, X. J., Mariotti, L., and Shi, Y., 2011: Higher hydroclimatic intensity with global warming. *J. Clim.*, 24, 5309 – 5324. doi:10.1175/2011JCLI3979.1.

Hanafusa, M., Sasaki, H., Murata, A. & Kurihara, K., 2013: Projection of Changes in Future Surface Wind around Japan Using a Non-hydrostatic Regional Climate Model. *SOLA*, 9, 23–26

Hartmann, D. L., 2016: Global Physical Climatology (Second Edition). Elsevier Science.

Hill, T. & Lewicki, P., 2006: Statistics: methods and applications: a comprehensive reference for science, industry, and data mining. *StatSoft*.

Hirahara, S., Ishii, M., & Fukuda, Y., 2014: Centennial-scale sea surface temperature analysis and its uncertainty. *J. Clim.* 27:57-75. doi:10.1175/JCLI-D-12-00837.1.

Hirai, M., & Oh'izumi, M., 2004: Development of a new land-surface model for JMA-GSM. *Extended abstract of 20th Conference on Weather Analysis and Forecasting/16th Conference on Numerical Weather Prediction*, P2.22.

Hori, M. E., & Ueda, H., 2006: Impact of global warming on the East Asian winter monsoon as revealed by nine coupled atmosphere-ocean GCMs. *Geophys. Res. Lett.,* 33, L03713.

Hosaka, M., Nohara, D., and Kitoh, A., 2005: Changes in snow cover and snow water equivalent due to global warming simulated by a 20km-mesh global atmospheric model. *SOLA*, 1, 93-96

Hosking, J. R. M., & Wallis, J. R., 1997: Regional Frequency Analysis: An Approach based on L-moments. *Cambridge University Press, Cambridge*, 224 pp.

Hu, Z. Z., Bengtsson, L., & Arpe, K., 2000: Impact of the global warming on the Asian winter monsoon in a coupled GCM. *J. Geophys. Res.,* 105, 4607–4624.

Hueging, H., Haas, R., Born, K., Jacob, D., & Pinto, J. G., 2013: Regional changes in wind energy potential over Europe using regional climate model ensemble projections. *J. Appl. Meteorol. Climatol.,* 52, 903–917.

Iizumi, T., Nishimori, M., Dairaku, K. Adachi, S. A., & Yokozawa, M., 2011: Evaluation and intercomparison of downscaled daily precipitation indices over Japan in present-day climate: Strengths and weaknesses of dynamical and biascorrection-type statistical downscaling methods. *J. Geophys. Res. Atmos.*, 116, D01111, doi:10.1029/2010JD014513.

Ikeda, K., Rasmussen, R., Liu, C., Gochis, D., Yates, D., Chen, F., Tewari, M., Barlage, M., Dudhia, J., Miller, K., Arsenault, K., Grubišić, V., Thompson, G., & Guttman, E., 2010: Simulation of seasonal snowfall over Colorado. *Atmos. Res.,* 97, 462–477.

Ishida, J., Aranami, K., Kawano, K., Matsubayashi, K., Kitamura, Y., & Muroi, C. 2022: ASUCA: the JMA operational non-hydrostatic model. *J. Meteor. Soc. Japan*, 100. doi.org/10.2151/jmsj.2022-043

Ishizaki, N., & Takayabu, I., 2009: On the Warming Events over Toyama Plain by Using NHRCM. *SOLA*, 5, 129-132

Ito, R., Aoyagi, T., Hori, N., Oh'izumi, M., Kawase, H., Dairaku, K., Seino, N., & Sasaki, H., 2018: Improvement of Snow Depth Reproduction in Japanese Urban Areas by the Inclusion of a Snowpack Scheme in the SPUC Model. *J. Metor. Soc. Japan*, 96, 511.534. doi.org/10.2151/jmsj.2018-053

Kawase, H., Yoshikane, T., Hara, M., Fujita, M., Ishizaki, N., Hatsushika H., & Kimura, F., 2012: Downscaling of snow cover changes in the late 20th Century using a past climate simulation method over Central Japan. *SOLA*, 8, 61-64.

Kawase, H., Sasaki, H., Murata, A., Nosaka, M., & Ishizaki, N. N., 2015: Future changes in winter precipitation around Japan projected by ensemble experiments using NHRCM. *J. Metor. Soc. Japan*, 93, 571.580.

Kawase, H., Murata, A., Mizuta, R., Sasaki, H., Nosaka, M., Ishii, M., & Takayabu, I., 2016: Enhancement of heavy daily snowfall in central Japan due to global warming as projected by large ensemble of regional climate simulations. *Climatic Change*, 139(2), 265–278.

Kawase, H., Iida, H., Aoki, K., Shimada, W., Nosaka, M., Murata, A., & Sasaki, H., 2019: Comparison of snow cover observations along the Tateyama-Kurobe Alpine route with snow cover simulations using the non-hydrostatic regional climate model (NHRCM) with different horizontal resolutions. *J. Geogr (Chigaku Zasshi)* 128:77–92 (in Japanese with English abstract).

Kawase, H., Yamazaki T., Sugimoto, S., Sasai, T., Ito, R., Hamada, T., Kuribayashi, M., Fujita, M., Murata, A., Nosaka, M., & Sasaki, H., 2020a: Changes in extremely heavy and light snow-cover winters due to global warming over high mountainous areas in central Japan. *PEPS.* doi.org/10.1186/s40645-020-0322-x

Kawase, H., Murata, A., Yamada, K., Nakaegawa, T., Ito, R., Mizuta, R., Nosaka, M., Watanabe, S., & Sasaki, H., 2020b: Regional characteristics of future changes in snowfall in Japan under RCP2.6 and RCP8.5 scenarios. *SOLA*, 17, 1-7.

Kitoh, A., & Endo, H., 2019: Future changes in precipitation extremes associated with tropical cyclones projected by large-ensemble simulations. *J. Metor. Soc. Japan*, 97, 141–152.

Kimoto, M., 2005: Simulated change of the East Asian circulation under global warming scenario. *Geophys. Res. Lett*., 32, L16701.

Kodama, C., Yamada, Y., Noda, A. T., Kikuchi, K., Kajikawa, Y., Nasuno, T., Tomita, T., Yamaura, T., Takahashi, T. G., Hara, M., Kawatani, Y., Satoh, M., & Sugi, M. 2015: A 20-year climatology of a NICAM AMIP-type simulation. *J. Meteor. Soc. Japan*, 93, 393-424, doi:10.2151/jmsj.2015-024.

Kuno, R., & Inatsu, M., 2014: Development of sampling downscaling: A case for wintertime precipitation in Hokkaido. *Climate Dyn*., 43, 375-387.

Kurihara, K., Ishihara, K., Sasaki, H., Fukuyama, Y., Saitou, H., Takayabu, I., Murazaki, K., Sato, Y., Yukimoto, S., & Noda, A., 2005: Projection of climatic change over Japan due to global warming by high resolution regional climate model in MRI. *SOLA*, 1, 97−100, doi:10.2151/sola.2005-026.

Lee, D., Min, S. K., Fischer, E., Shiogama, H., Bethke, I., Lierhammer, L., & Scinocca, J. F., 2018: Impacts of half a degree additional warming on the Asian summer monsoon rainfall characteristics. *Environ. Res. Lett.,* 13. doi:10.1088/1748-9326/aab55d, 044033.

Leduc, M., Mailhot, A., Frigon, A., Martel, J.-L., Ludwig, R., Brietzke, G. B., Giguère, M., Brissette, F., Turcotte, R., Braun, M., and Scinocca, J., 2019: ClimEx project: a 50-member ensemble of climate change projections at 12-km resolution over Europe and northeastern North America with the Canadian Regional Climate Model (CRCM5). *J. Appl. Meteorol. Climatol.* 58:663-693. doi:10.1175/jamc-d-18-0021.1.

Lin, Y. H., Farley, R. D., & Orville, H. D., 1983: Bulk parameterization of the snow field in a cloud model. *J. Clim. Appl. Meteor.* 22:1065-1092

Liu, W., Sun, F., Lim, W. H., Zhang, J., Wang, H., Shiogama, H., & Zhang, Y., 2018: Global drought and severe drought-affected populations in 1.5 and 2 °C warmer worlds. *Earth Syst. Dynam.,* 9:267-283. doi:10.5194/esd-9-267-2018.

Lute, A. C., Abatzoglou, J. T., & Hegewisch, K. C., 2015: Projected changes in snowfall extremes and interannual variability of snowfall in the western United States. *Water Resour. Res.,* 51, 960.972. doi:10.1002/2014WR016267

Masson-Delmotte, V., Zhai, P., Pörtner, H.-O., Roberts, D., Skea, J., Shukla, P.R., Pirani, A., Moufouma-Okia, W., Péan, C., Pidcock, R., Connors, S., Matthews, J.B.R., Chen, Y., Zhou,

X., Gomis, M.I., Lonnoy, E., Maycock, T., Tignor, M., & Waterfield, T., (Eds.), 2018: *Special Report on Global Warming of 1.5 ℃.* World Meteorological Organization.

Matsumura, S., & Sato, T., 2011: Snow/ice and cloud responses to future climate change around Hokkaido. *SOLA*, 7, 205–208.

Mclnnes, K. l., Erwin, T. A., & Bathols, J. M., 2011: Global Climate Model projected changes in 10m wind speed and diraction due to anthropogenic climate change. *Atmos. Sci. Lett.,* 12, 325–333.

Met Office Hadley Centre ,2018: UKCP18 Probabilistic Climate Projections. Centre for Environmental Data Analysis, date of citation.

Mitchell, D., R. James, P. Forster, R. Betts, H. Shiogama, & M. Allen, 2016: Realizing the impacts of a 1.5 °C warmer world. *Nat. Clim. Change,* 6:735-737. doi:10.1038/nclimate3055.

Mitchell, D., AchutaRao, K., Allen, M., Bethke, I., Beyerle, U., Ciavarella, A., Forster, P. M., Fuglestvedt, J., Gillett, N., Haustein, K., Ingram, W., Iversen, T. Kharin, V., Klingaman, N., Massey, N., Fischer, E., Schleussner, C. F., Scinocca, J., Seland, Ø., Shiogama, H., Shuckburgh, E., Sparrow, S., Stone, D., Uhe, P., Wallom, D., Wehner, M., & Zaaboul., R., 2017: Half a degree additional warming, prognosis and projected impacts (HAPPI): background and experimental design. *Geosci. Model Dev.,* 10:571-583. doi:10.5194/gmd-10-571-2017.

Miyamoto, Y., Y. Kajikawa, R. Yoshida, T. Yamaura, H. Yashiro, and H. Tomita, 2013: Deep moist atmospheric convection in a subkilometer global simulation, *Geophys. Res. Lett.*, 40, 4922-4926.

Mizuta, R., Yoshimura, H., Murakami, H., Matsueda, M., Endo, H., Ose, T., Kamiguchi, K., Hosaka, M., Sugi, M., Yukimoto, S., Kusunoki S., & Kitoh, A., 2012: Climate simulations using the improved MRIAGCM with 20-km grid. *J. Metor. Soc. Japan*, 90A, 233−258.

Mizuta, R., Arakawa, O., Ose, T., Kusunoki, S., Endo, H., & Kitoh, A., 2014: Classification of CMIP5 future climate responses by the tropical sea surface temperature changes. *SOLA*, 10, 167–171.

Mizuta, R., Murata, A., Ishii, M., Shiogama, H., Hibino, K., Mori, N., Arakawa, O., Imada, Y., Yoshida, K., Aoyagi, T., Kawase, H., Mori, M., Okada, Y., Shimura, T., Nagatomo, T., Ikeda, M., Endo, H., Nosaka, M., Arai, M., Takahashi, C., Tanaka, K., Takemi, T., Tachikawa, Y., Temur, K., Kamae, Y., Watanabe, M., Sasaki, H., Kitoh, A., Takayabu, I., Nakakita, E., & Kimoto, M., 2017: Over 5000 years of ensemble future climate simulations

by 60 km global and 20 km regional atmospheric models. *Bull. Amer. Meteor. Soc.,* 98:1383-1398. doi:10.1175/BAMS-D-16-0099.1.

Mori, N., Shimura, T., Yoshida, K., Mizuta, R., Okada, Y., Fujita, M., Khujanazarov, T., & Nakakita, E., 2019: Future changes in extreme storm surges based on mega-ensemble projection using 60-km resolution atmospheric global circulation model. *Coastal Engineering Journal*, Taylor & Francis, 13p.

Mott, R., Vionnet, V., & Grünewald, T., 2018: The Seasonal Snow Cover Dynamics: Review on Wind-Deiven Coupling Processes. *Front. Earth Sci.,* doi:10.3389/feart.2018.00197

Murakami, M., 1990: Numerical modeling of dynamical and microphysical evolution of an isolated convective cloud. The 19 July 1981 CCOPE cloud. *J. Metor. Soc. Japan,* 68:107-128

Murakami, M., Clark, T.L., & Hall, W.D., 1994: Numerical simulation of convective snow clouds over the Sea of Japan: two-dimensional simulation of mixed layer development and convective snow cloud formation. *J. Metor. Soc. Japan,* 72:43-62

Murata, A., Sasaki, H., Kawase, H., Nosaka, M., Oh'izumi, M., Kato, T., Aoyagi, T., Shido, F., Hibino, K., Kanada, S., Suzuki-Parker, A., & Nagatomo, T., 2015: Projection of Future Climate Change over Japan in Ensemble Simulations with a High-Resolution Regional Climate Model. *SOLA*, 11, 90–94, doi:10.2151/sola.2015-022

Murata, A., Sasaki, H., Kawase, H., Nosaka, M., Aoyagi, T., Ohizumi, M., Seino, N., Shido, F., Hibino, K., Ishihara, K., Murai, H., Yasui, S., Wakamatsu, S., & Takayabu, I., 2017: Projection of Future Climate Change over Japan in Ensemble Simulations Using a Convection-Permitting Regional Climate Model with Urban Canopy. *SOLA*, 13, 219–223.

Nishimori, M., Ishigooka, Y., Kuwagata, T., Takimoto, T., & Endo, N., 2019: SI-CAT 1km-grid square Regional Climate Projection Scenario Dataset for Agricultural Use (NARO2017). *Journal of The Japan Society for Simulation Technology*, 38, 150-154 (in Japanese with English title).

Onogi, K., Tsutsui, J., Koide, H., Sakamoto, M., Kobayashi, S., Hatsushika, H., Matsumoto, T., Yamazaki, N., Kamahori, H., Takahashi, K., Kadokura, S., Wada, K., Kato, K., Oyama, R., Ose, T., Mannoji, N., & Taira, R., 2007: The JRA-25 Reanalysis. *J. Metor. Soc. Japan,* 85, 369-432, doi:10.2151/jmsj.85.369.

Ose, T., 2019: Characteristics of future changes in summertime East Asian monthly precipitation in MRI-AGCM global warming experiments. *J. Metor. Soc. Japan,* 97:317-335. doi:10.2151/jmsj.2019-018.

Overland, J. E., & Wang, M., 2010: Large-scale atmospheric circulation changes are associated with the recent loss of Arctic sea ice. *Tellus*, A, 62, 1–9.

Pendergrass, A.G., Knutti, R., Lehner, F., Deser, C., & Sanderson B. M., 2017: Precipitation variability increases in a warmer climate. *Sci. Rep.,* 7, 17966 2017. https://doi.org/10.1038/s41598-017-17966-y

Piazza, M., Boé, J., Terray, L., Pagé, C., Sanchez-Gomez, E., & Déqué, M., 2014: Projected 21st century snowfall changes over the French Alps and related uncertainties. *Climate Change*, 122, 583-594, doi:10.1007/s10584-013-1017-8.

Rasmussen, R., Liu, C., Ikeda, K., Gochis, D., Yates, D., Chen, F., Tewari, M., Barlage, M., Dudhia, J., Yu, W., & Miller, K., 2011: High-resolution coupled climate runoff simulations of seasonal snowfall over Colorado: a process study of current and warmer climate. *J. Clim.*, 24, 3015–3048.

Salathé, EP, Leung, L.R., Qian, Y., & Zhang, Y., 2010: Regional climate model projections for the state of Washington. *Climatic Change*, 2010;102:51–75.

Sasaki, H., Kurihara K., Takayabu, I., & Uchiyama, T., 2008: Preliminary experiments of reproducing the present climate using the non-hydrostatic regional climate model. *SOLA*, 4, 25−28.

Sasaki, H., Murata, A., Hanafusa, M., Oh'izumi, M., & Kurihara, K., 2011: Reproducibility of present climate in a non-hydrostatic regional climate model nested within an atmosphere general circulation model. *SOLA*, 7:173-176. doi:10.2151/sola.2011-044.

Sasaki, H., Murata, A., Hanafusa, M., Oh'izumi, M., & Kurihara, K., 2012: Projection of future climate change in a nonhydrostatic regional climate model nested within an atmospheric general circulation model. *SOLA*, 8, 53−56, doi:10.2151/sola.2012-014.

Sasaki, H., Kurihara, K., Murata, A., Hanafusa, M., & Oh'izumi, M., 2013: Future changes of snow depth in a non-hydrostatic regional climate model with bias correction. *SOLA*, 9, 05−08, doi:10.2151/sola.2013-002.

Sato, T., & Sugimoto, S., 2013: A numerical experiment on the influence of the interannual variation of sea surface temperature on terrestrial precipitation in northern Japan during the cold season. *Water Resour. Res.,* 49, 7763–7777. doi:10.1002/2012WR013206

Scherrer, S. C., Ceppi, P., Croci-Maspoli, M., & Appenzeller, C., 2012: Snow-albedo feedback and Swiss spring temperature trends. *Theor. Appl. Climatol.*, 110, 509–516.

Shi, X., & Durran, D., 2016: Sensitivities of Extreme Precipitation to Global Warming Are Lower over Mountains than over Oceans and Plains. *J. Clim.*, 29, 4779-4791, doi:10.1175/JCLI-D-15-0576.1

Shiogama, H., Emori, S., Takahashi, K., Nagashima, T., Ogura, T., Nozawa, T., & Takemura, T., 2010: Emission scenario dependency of precipitation on global warming in the MIROC3.2 model. *J. Clim.*, 23, 2404–2417, doi:10.1175/2009JCLI3428.1.

Shiogama, H., Hasegawa, T., Fujimori, S., Murakami, D., Takahashi, K., Tanaka, K., Emori, S., Kubota, I., Abe, M., Imada, Y., Watanabe, M., Mitchell, D., Schaller, N., Sillmann, J., Fischer, E. M., Scinocca, J. F., Bethke, I., Lierhammer, L., Takakura, J., Trautmann, T., Döll, P., Ostberg, S., Schmied, H. M., Saeed, F., & Schleussner, C. F., 2019: Limiting global warming to 1.5 °C will lower increases in inequalities of four hazard indicators of climate change. *Environ. Res. Lett.,* 14. doi:10.1088/1748-9326/ab5256, 124022.

Takahashi, H. G., & Idenaga, T., 2013: Impact of SST on precipitation and snowfall on the Sea of Japan side in the winter monsoon season: Timescale dependency. *J. Metor. Soc. Japan*, 91, 639–653. doi:10.2151/jmsj.2013-506

Takayabu, I., & Hibino, K., 2016: The skillful time scale of climate models. *J. Metor. Soc. Japan,* 94A:191-197. doi:10.2151/jmsj.2015-038.

Takemi, T., 2013: High-Resolution Meteorological Simulations of Local-Scale Wind Fields over Complex Terrain: A Case Study for the Eastern Area of Fukushima in March 2011. *Theoretical and Applied Mechanics Japan*, 61, 3-10.

Trenberth, K.E., 2011: Changes in precipitation with climate change. *Clim. Res*., 47, 123 – 138, doi:10.3354/cr00953.

von Trentini F., Leduc, M., & Ludwig, R., 2019: Assessing natural variability in RCM signals: comparison of a multi model euro-CORDEX ensemble with a 50-member single model large ensemble. *Clim. Dyn.,* 53:1963-1979. doi:10.1007/s00382-019-04755-8.

Shi, X., & Durran, D., 2016: Sensitivities of Extreme Precipitation to Global Warming Are Lower over Mountains than over Oceans and Plains. *J. Clim.*, 29, 4779–4790.

Wang, G., Wang, D., Trenberth, K.E., Erfanian, A., Yu, M., Bosilovich, M., & Parr, D.T., 2017: The peak structure and future changes of the relationships between extreme precipitation and temperature. *Nat. Clim. Chang,* 7:268-274. doi:10.1038/nclimate3239.

Wang, A., Xu, L., & Kong, X., 2018: Assessments of the Northern Hemisphere snow cover response to 1.5 and 2.0 °C warming. *Earth Syst. Dynam*., 9, 865–877.

Yasunaga, K., & Tomochika, M., 2017: An increasing trend in the early winter precipitation during recent decades along the coastal areas of the Sea of Japan. *J. Hydrometeor*., 18, 2893-2906, doi:10.1175/JHM-D-17-0105.1.

Yoshida, K., Sugi, M., Mizuta, R., Murakami, H., & Ishii, M., 2017: Future changes in tropical cyclone activity in high-resolution large-ensemble simulations. *Geophys. Res. Lett.*, 44, 9910-9917.